Electronic Supplementary Information (ESI) for

Small Molecule-based Supramolecular-Polymer Double-Network Hydrogel Electrolytes for Ultra-Stretchable and Waterproof Zn–air Batteries Working from –50 to 100 °C

Chaonan Gu,[†a] Xiao-Qiao Xie,[†a] Yujia Liang,[a] Jingjing Li,[*b] Hai Wang,[a] Kaifang Wang,[a]

Junpeng Liu,[a] Mengke Wang,[a] Yunfei Zhang,[a] Manxing Li,[a] Huajie Kong[a] and Chun-Sen Liu[*a]

[a]Henan Provincial Key Lab of Surface & Interface Science, Zhengzhou University of Light Industry, Zhengzhou, 450001, China. E-mail: chunsenliu@zzuli.edu.cn

[b]School of Chemistry and Chemical Engineering, Henan University of Technology, Zhengzhou, 450001, China.

E-mail: nicoleljj@tju.edu.cn

[†]These authors contributed equally to this work.

1

Table of Contents

Video S1

Simulated assembly mechanism of the G-CyBA/PAAm SP-DN hydrogel based on theoretical calculations, showing multiple hydrogen-bonding interactions within supramolecular network and between individual supramolecular and polymer networks.

Video S2

Biaxial tension test of the square G-CyBA/PAAm SP-DN hydrogel, showing over 4000% areal strain (from 3.0×3.0 cm^2 to 19×19 cm^2).

Video S3

Anti-freezing performance of 600%-KOH (6 M)-filled G-CyBA/PAAm SP-DN hydrogel at -80 ^{o}C (dry ice), which can be stretched reversibly.

Video S4

Anti-freezing performance of 600%-KOH (6 M)-filled G-CyBA/PAAm SP-DN hydrogel at -196 ^{o}C (liquid nitrogen), which can quickly revival from a frozen state to a stretchable state within 2 minutes.

Video S5

Comparison between the adhesiveness of 600%-KOH (6 M)-filled G-CyBA/PAAm SP-DN and KOH (6 M)-filled PAAm SN hydrogels to zinc sheet or carbon nanotube paper, respectively.

Video S6

Conformal stretching of 600%-KOH (6 M)-filled SP-DN hydrogel adhered to a zinc spring by physical attachment, which can withstand multiple cycles of conformal stretching over 1000% strain without detaching from each other.

Video S7

The manufacturing process of the super-stretchable Zn–air battery based on the 600%-KOH (6 M)-filled G-CyBA/PAAm SP-DN hydrogel electrolyte.

Video S8

Ultra-low temperature resistance of the Zn–air battery, which can survive and work well even down to −100 °C during at least 5 cooling-warming cycles.

Video S9

Waterproof performance of the as-prepared Zn–air battery without any special treatment, which can power a light-emitting diode (LED) for over 25 min under continuous rinsing by tap water.

Video S10

Highly stretchability and temperature-tolerance of the Zn–air battery, which can easily withstand over 1000% strain and keep reliable power output to light up a LED during stretching process under various temperatures (RT, −40 and 70 ºC).

Video S11

Wearable performance of the fabric Zn–air battery, which can be woven into flexible textiles to effectively charge a smartphone even when bended, folded and twisted.

Section S1 Methods

1. Materials

Guanosine (G, 98%) was purchased from Alfa aesar, KOH (99.98%) was purchased from Acros Organics Co., Ltd., Cyclohexylboronic acid (CyBA, 97%) and Boric acid (BA, ≥ 99.5%) were purchased from Shanghai Aladdin Biochemical Technology Co., Ltd., Phenylboronic acid (PBA, > 98%) was purchased from Shanghai Adamas Reagent Co., Ltd., Acrylamide (AAm, 99%) was purchased from J&K Scientific Ltd. 2-Hydroxy-4'-(2-hydroxyethoxy)-2-methylpropiophenone (Irgacure 2959, 98%) and *N,N'*-Methylenebis(acrylamide) (MBA, 97%) were purchased from Beijing InnoChem Science&Technology Co., Ltd., Carbon nanotube (CNT) paper and carbon cloth were purchased from Suzhou Tanfeng Graphene Technology Co., Ltd., Zinc wire (0.5 mm in diameter, purity > 99.99%), zinc sheet (thickness of 0.3 mm ,purity > 99.99%), stainless steel (304) and nickel foam (thickness of 0.3 mm) were purchased from Sinopharm Chemical Reagent Co. Ltd. All other chemicals used in this work were commercially analytical grade reagents without further purification.

2. Instruments

Nuclear magnetic resonance (NMR) measurements were performed on a 500 MHz NMR spectrometer (JEOL ECZ600R/S3). All ^{11}B NMR spectra were obtained at 192.43 MHz. The ^{11}B background signal from the NMR probe and the NMR tube was removed by performing backward linear FID prediction. The chemical shift reference of ^{11}B NMR and ^{1}H NMR was BF$_3$OEt$_2$ and TMS. Powder X-ray diffraction (PXRD) profiles were performed using a Bruker D8 Advance X-ray diffractometer using Cu Kα radiation at 25 °C. Fourier transform infrared (FT-IR) spectra of the samples were measured by Nicolet 5700 FT-IR. Circular dichroism (CD) of the hydrogels were analyzed on a Chirascan CD spectrometer. Three scans were performed from 200 to 500 nm for each sample. Rheological tests were performed by using a Hake Mars rheometer (Thermo Scientific) at 25 ºC with a parallel plate geometry (40 mm, 1 mm gap). The tensile test and lap-shear test was performed on a UTM2202 electronic universal testing machine. UV-visible spectrum was recorded on a HITACHI

UH4150 spectrophotometry. The galvanostatic charge and discharge test was carried out by using the LANHE testing system. All the electrochemistry tests were measured by using the Solartron Analytical Modulab XM CHAS 08 electrochemical workstation.

3. Preparation of G-CyBA/PAAm supramolecular-polymer double-network (SP-DN) hydrogels

The SP-DN hydrogels were synthesized by a simple and facile one-pot method. The composition of the SP-DN hydrogels were referred to as (G-CyBA)$_x$-AAm$_y$-MBA$_z$-t, where x is the mass of guanosine (G, mg), y is the mass of acrylamide (AAm, mg), z is the volume of *N,N'*-methylenebis(acrylamide) (MBA) aqueous (µL), and t is the irradiation time (min) of UV lamp (wavelength of 365 nm, intensity of 0.4 W cm^{-2}). The G: CyBA: KOH molar ratio was 1:1:1, the mass of Irgacure 2959 was 22.4 mg, and the volume of distilled water was 1.0 mL. Briefly, as for synthesis of the targeted G-CyBA/PAAm SP-DN hydrogel, namely (G-CyBA)$_{80}$-AAm$_{500}$-MBA$_{46}$-30, 80.0 mg of G (0.28 mmol), 36.1 mg of CyBA (0.28 mmol), 500.0 mg of AAm (7.03 mmol), 46 µL of MBA aqueous (10 mg mL^{-1}), and 22.4 mg of Irgacure 2959 (0.1 mmol) were added to a reaction cell, followed by adding 1.0 mL KOH aqueous solution (0.28 mol L^{-1}). The vial was heated at 90 °C for 5 min to completely dissolve the reactants and to allow the formation of G-CyBA borate esters. The obtained homogenous solution was then quickly poured into suitable molds, covered with a transparent glass and then cooled to room temperature to favor the G-CyBA gelation. After aging for a few minutes, the molds were irradiated with a UV lamp with the wavelength of 365 nm and the intensity of 0.4 W cm^{-2} for ~30 min to allow the polymerization of AAm monomers, thus leading to the formation of G-CyBA/PAAm SP-DN hydrogel. Other SP-DN hydrogels with different compositions were also prepared following the similar procedure mentioned above. The PAAm polymer single-network (SN) hydrogel was also synthesized using the same process, but without the addition of G, CyBA, and KOH. In contrast to most polymer gels, which require repeated degassing to ensure the free radical polymerization reaction, herein, the degassing was not necessary for preparation of the SP-DN hydrogels. KOH-filled hydrogels were obtained by immersing the as-prepared hydrogels in different

concentrations of KOH (aq.) for swelling.

4. Fabrication of the flexible and ultra-stretchable Zn–air batteries (ZABs)

The air cathode was fabricated by drop-casting the Co@N-PCP/NB-CNF-2-800 catalyst, reported in our previous work,[1] onto a carbon nanotube (CNT) paper with a mass loading of 1.0 mg cm^{-2}. The anode was fabricated using a zinc spring by coiling a zinc wire with the diameter of 0.5 mm. KOH (6 M)-filled G-CyBA/PAAm SP-DN hydrogel with 600% swelling ratio was used as both electrolyte and separator. Flexible ZABs were assembled by sandwiching the Zn anode, the hydrogel electrolyte, and the air cathode together, which was reinforced and protected by using a punched heat shrinking tubing (Fig. S25). For stretchable ZABs (Fig. 5a, Fig. S25 and Video S7), the hydrogel electrolyte coated Zn-spring was pre-stretched to ca. 1200% strain, followed by wrapping the air cathode by physical attachment. After release, an ultra-stretchable ZAB was successfully obtained. Due to the robust interfacial adhesion of the hydrogel, the anode and cathode were firmly adhered to the hydrogel electrolyte for accommodating a large deformation.

5. Computer simulations

Conformational search was first carried out for G-CyBA monomers and representative PAAm (10 units) segments. The geometry optimization and frequency analysis of the stable isomers were performed with SMD solvation model in water solvent, using B3LYP functional and 6-31+G(d,p) basis set with DFT-D3(BJ) dispersion correction. After that, the most stable isomers were selected (Figs. S5 and S6) as building blocks to construct the models of the supramolecular species and supramolecular-polymer double-network species. Geometry optimization of these species was performed using the semi-empirical PM7 method.[2,3] The recently developed PM7 method has included dispersion and hydrogen-bond corrections, allowing for a better description of non-covalent interactions, especially hydrogen bonding. Moreover, PM7 is considered to be suitable for modeling a wide range of species, particularly when the size of the system is computationally demanding for DFT methods. The single point energies were calculated using B3LYP functional and 6-31+G(d,p) basis set with

DFT-D3(BJ) dispersion correction on the optimized geometries.[4] All calculations were performed with Gaussian 09.[5] Computed structures were illustrated using CYLView. Cartesian coordinates of the optimized G-CyBA/PAAm SP-DN structure are shown in Table S12 (a .xls file).

6. Mechanical test

The tensile properties of the hydrogels were carried out using a universal test machine (UTM2202) with a 100 N load cell at a constant velocity of 100 mm min^{-1} in air. The G-CyBA/PAAm SP-DN hydrogels and PAAm single-network (SN) hydrogels were cut into a dumbbell-shape with the ISO 37:2011 standard size. For cycle test, the SP-DN hydrogel was first stretched to a fixed strain (500%) at a velocity of 100 mm min^{-1} and then unload immediately with the same speed. Without waiting, the samples were subject to another cycle test. The dissipated energies (U_{hys}) were calculated from the area between loading-unloading curves. For tearing test, the samples were cut into the standard ISO 34-1:2004 1/2 sizes ($50 \times 15 \times 2.0$ mm^3) with an initial notch of 20 mm. The two arms of the specimens were clamped with the gauge length of 10 mm, in which the lower one was fixed, while the upper one was pulled at a constant velocity of 100 mm min^{-1}. The tearing energy T was calculated at a constant tearing force F using the relation $T = 2F_{av}/w$, Where F_{av} is the average force of peak values during steady-state tear and w is the thickness of the sample.[6,7]

For tensile test of the KOH-filled hydrogels, the samples were cut into a rectangular-shape (40 mm in length, 6 mm in width, and 2 mm in thickness) before soaking. Upon swelling, the width and thickness of the KOH-filled hydrogels was re-measured by a vernier caliper. The two arms of the specimens were clamped with the gauge length of 10 mm, and subject for tensile test at a constant velocity of 100 mm min^{-1}.

To investigate the mechanical performance of the hydrogels after undergoing different temperatures, the samples were incubated under 100 °C for over 1 h and other desired temperatures (−80, −50, −40, 0, 60 and 70 °C) for at least 12 h. Then, the mechanical performance of these samples under different conditions was immediately tested after the samples were taken out. The ultra-low

temperature of −50 °C was controlled *via* a liquid nitrogen chamber, and the −80 °C was controlled by dry ice. Other temperatures were controlled *via* a freezer or an oven.

7. Adhesion test

The adhesion strength was determined by the lap-shear test using a universal test machine (UTM2202). A piece of KOH-filled SP-DN hydrogel were cut into 1.5 cm × 3.0 cm sample and sandwiched between two same substrates with or without backing layers by physical attachment. After applying a gentle pressure (~1 kPa) for ca. 1 h, the specimens were tested by the standard lap-shear test with a constant tensile speed of 10 mm min^{-1}. Adhesion strength was calculated by dividing the maximum force by the adhesion area.[8,9] Glass with 2 mm thickness was applied using double coated tapes as a stiff backing for soft substrates, such as carbon nanotube paper and carbon cloth. For other substrates such as zinc sheet, nickel foam, stainless steel, no backing layers were necessary. For temperature-resistant adhesion, the hydrogels were firstly incubated under −40 °C for over 12 h, and 100 °C for over 1 h, and then sandwiched by the substrates as describe above. At least three parallel samples were tested in each group.

8. Swelling measurement

The swelling ration (SR) of the hydrogels in different concentrations of aqueous KOH was characterized by the weight ratio of the swollen sample M to that of the as-prepared sample M_0, SR = M/M_0. To achieve adequate precision, at least three parallel samples were tested in each group.

9. Water retention ratio measurement

The water retention ratio (WR) of the hydrogels was determined by measuring the weights of the hydrogels and the dehydrated hydrogels. The water retention ratio (WR) was calculated using the relation WR = $(W_0 - W_1)/W_0$, where W_0 and W_1 are the weights of the water contained in the hydrogels and loss of water in the dehydrated hydrogels, respectively.

10. Conductivity measurement

Ionic conductivity of the hydrogels was measured by the electrochemical impedance spectroscopy

(EIS) method. Impedance data were obtained using a Solartron Analytical Modulab XM CHAS 08 electrochemical workstation in the frequency range of 0.001 to 100 kHz under a variety of temperatures of 100, 70, 60, RT, 0, –40, –50 and –80 °C. The ultra-low temperature of –50 °C was controlled *via* a liquid nitrogen chamber, and the –80 °C was controlled by dry ice. Other temperatures were controlled *via* a freezer or an oven. The hydrogels were incubated under 100 °C for over 3 h, and other desired temperatures for at least 12 h before sandwiched between two nickel foam for the measurement. The ionic conductivity of hydrogels was calculated according to the following equation.

$$\sigma = LR/A$$

where L is the thickness of the hydrogels, R is the impendence value and A is the contact area of the hydrogels, respectively.

11. Thermal characterization

Samples were characterized using a simultaneous thermal analysis (Netzsch, STA 449 F3 Jupiter). Samples were sealed in Pt pans (Netzsch, Platinum Hermetic Pan Φ 6.8 mm) for testing, with an empty pan used as inert reference. The DSC was operated under 30 mL min^{-1} helium flow rate. Samples were first equilibrated at 25 °C and then cooled at a rate of 5 °C min^{-1} to −185 °C. After an isothermal period of at least 120 min at −185 °C, samples were heated up at 10 °C min^{-1} to 40 °C, and data were captured at a rate of 1 Hz.

12. Electrochemical measurement

The open-circuit voltages, charge-discharge polarization and galvanostatic discharge curves of the ZAB were conducted using a Solartron Analytical Modulab XM CHAS 08 electrochemical workstation. The rate performance was determined at current densities of 1, 2, 4, 6, 8, and 10 mA cm^{-2}. The galvanostatic discharge and charge test was performed using a Land 2001A battery test system, at a fixed current density of 2 mA cm^{-2}, with each cycle consisting of 5 min for discharge followed by 5 min for charge.

The power densities of the ZAB were calculated according to the following equation:

$$P = V \times I$$

where I is the discharge current density and V is the corresponding voltage.

For temperature-dependent electrochemical performance, the flexible ZABs were tested at 100, 70, 25, −40 and −50 °C in a constant temperature chamber. The ultra-low temperature of −50 °C was controlled *via* a liquid nitrogen chamber, and the −80 °C was controlled by dry ice. Other temperatures were controlled *via* a freezer or an oven. For waterproof performance, *in situ* electrochemical test were performed by completely immersing the ZAB in water.

Section S2   **Characterization of G-CyBA/PAAm supramolecular-polymer double-network (SP-DN) hydrogel**
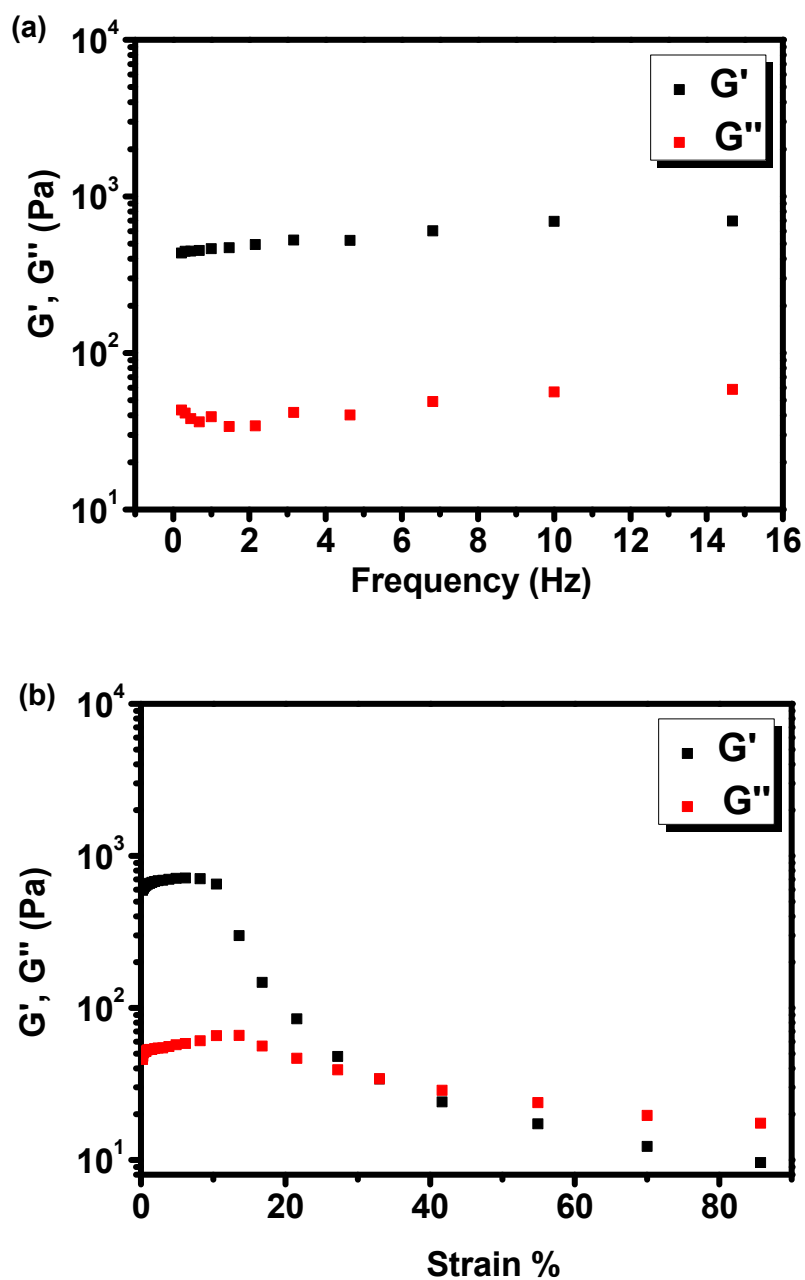
Fig. S1 The mechanical properties of G-CyBA/PAAm SP-DN hydrogel before photopolymerization. a,b) Dynamic frequency sweep (a) and oscillatory strain sweep (b). Rheological test demonstrated a typical elastic response of the storage modulus (G') and loss modulus (G'') of the hydrogels, as the G' is consistently higher than the G'', and is independent of frequency over the entire investigated range, confirming the gelation feature.
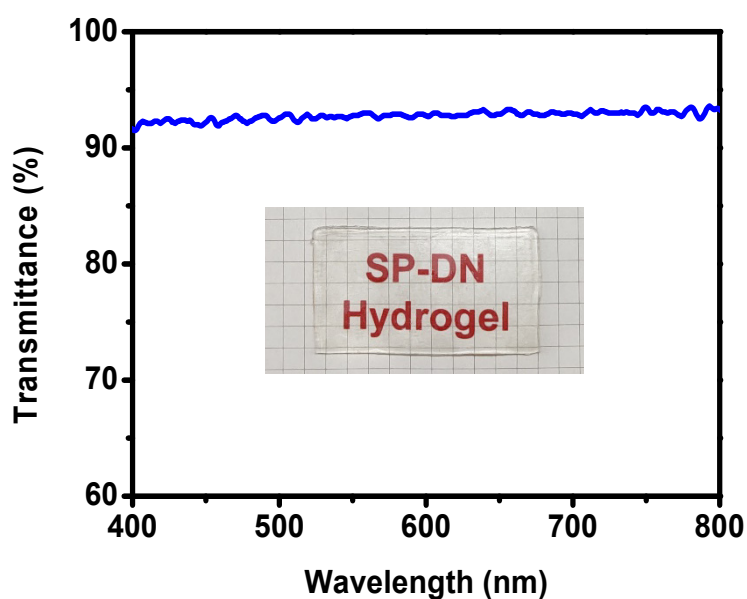
Fig. S2 Transparency of the as-prepared G-CyBA/PAAm SP-DN hydrogel. The transmittanc of the G-CyBA/PAAm SP-DN hydrogel is over 90% in the visible region. (Inset: experimental photo of the SP-DN hydrogel placed on grid paper).
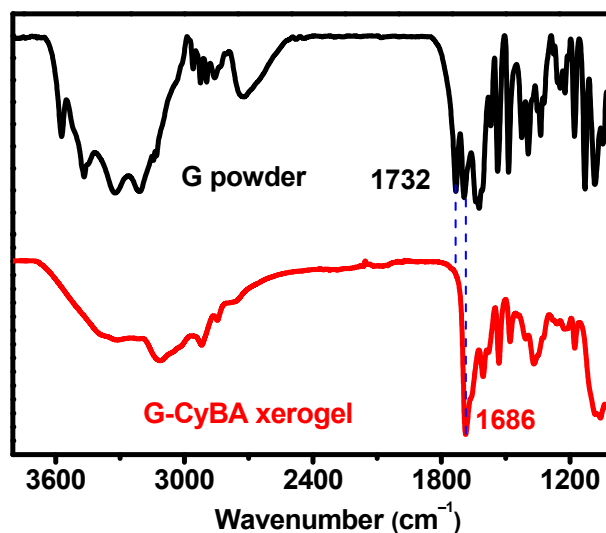
Fig. S3 FT-IR spectra of guanosine powder and lyophilized G-CyBA supramolecular hydrogel.
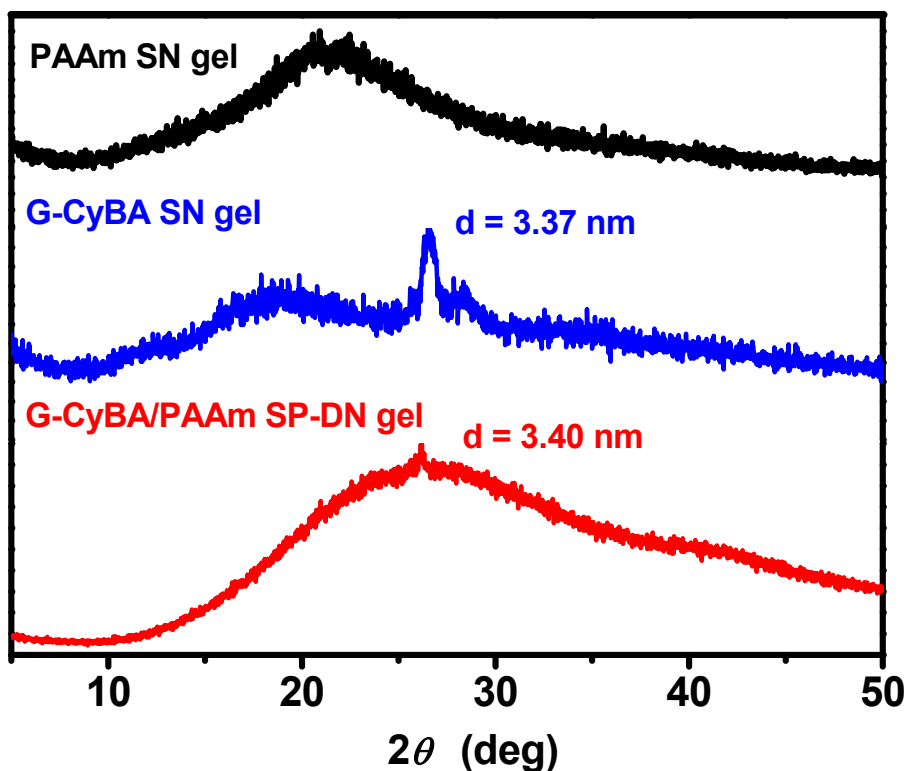
Fig. S4 XRD patterns of the lyophilized G-CyBA supramolecular hydrogel, PAAm polymer hydrogel and G-CyBA/PAAm SP-DN hydrogel. The strong diffraction peak at $2\theta = 26.44^{\circ}$ (d = 3.37 nm) in the G-CyBA supramolecular xerogel was correlated with the π–π stacking distance between adjacent G-quartets. The presence of typical characteristic peak of the G-CyBA supramolecualr network in the SP-DN hydrogel ($2\theta = 26.18^{\circ}$ and d = 3.40 nm) confirmed the successful incorporation of the supramolecular network into the polymer network.
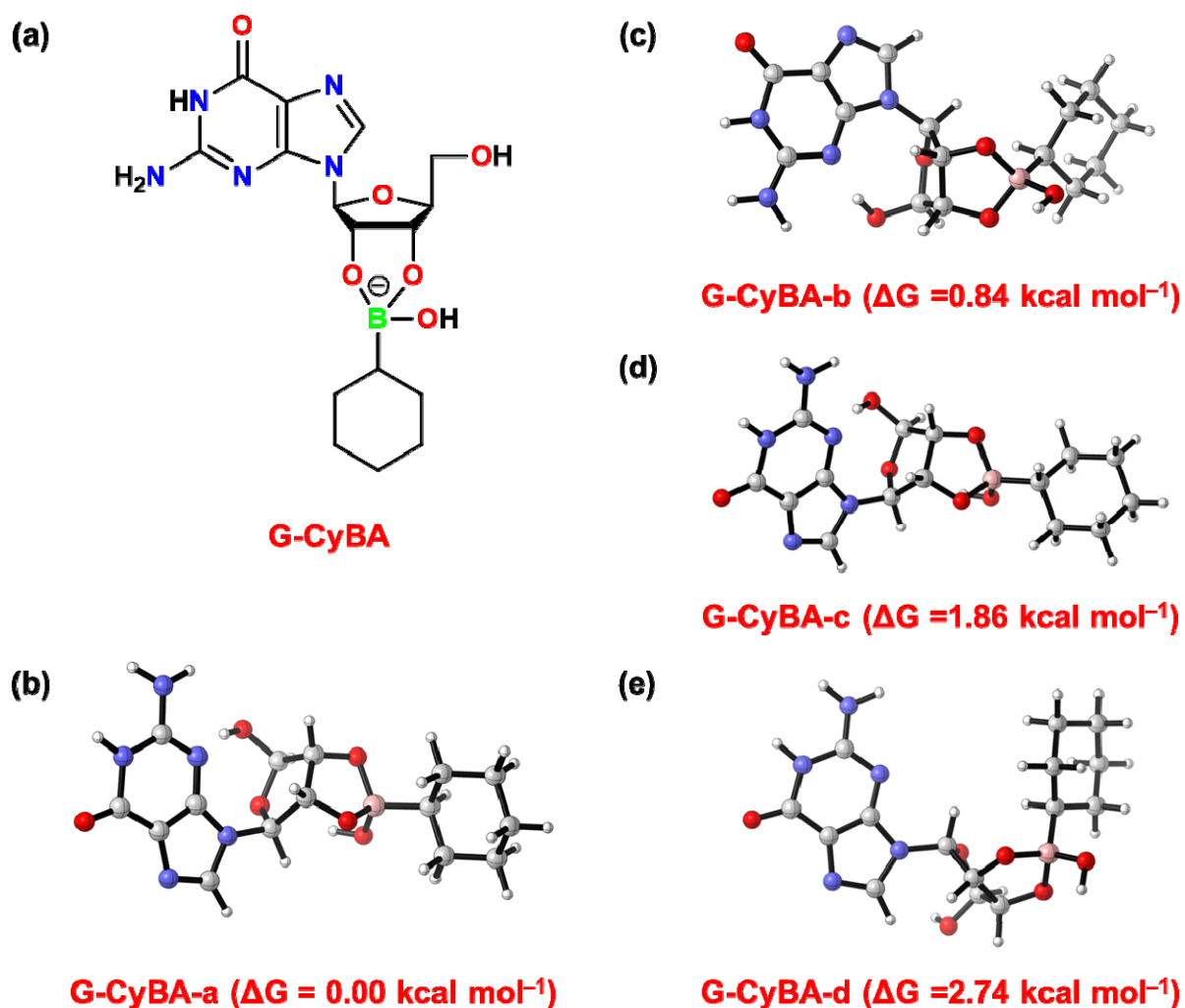
Fig. S5 Computer simulation of G-CyBA molecules. (a) Chemical structure of G-CyBA. (c-d) PM7 optimized geometries and calculated relative Gibbs free energy (ΔG) of the four most stable G-CyBA isomers. G-CyBA-a isomer with the lowest energy was selected to construct the supramolecular helical nanowire in the subsequent calculations.

(a) PAAm (10 units)

(b) PAAm-a (10 units) (ΔG = 0.00 kcal mol^{-1})

(c) PAAm-b (10 units) (ΔG = 7.18 kcal mol^{-1})

(d) PAAm-c (10 units) (ΔG = 16.49 kcal mol^{-1})

(e) PAAm-d (10 units) (ΔG = 20.71 kcal mol^{-1})
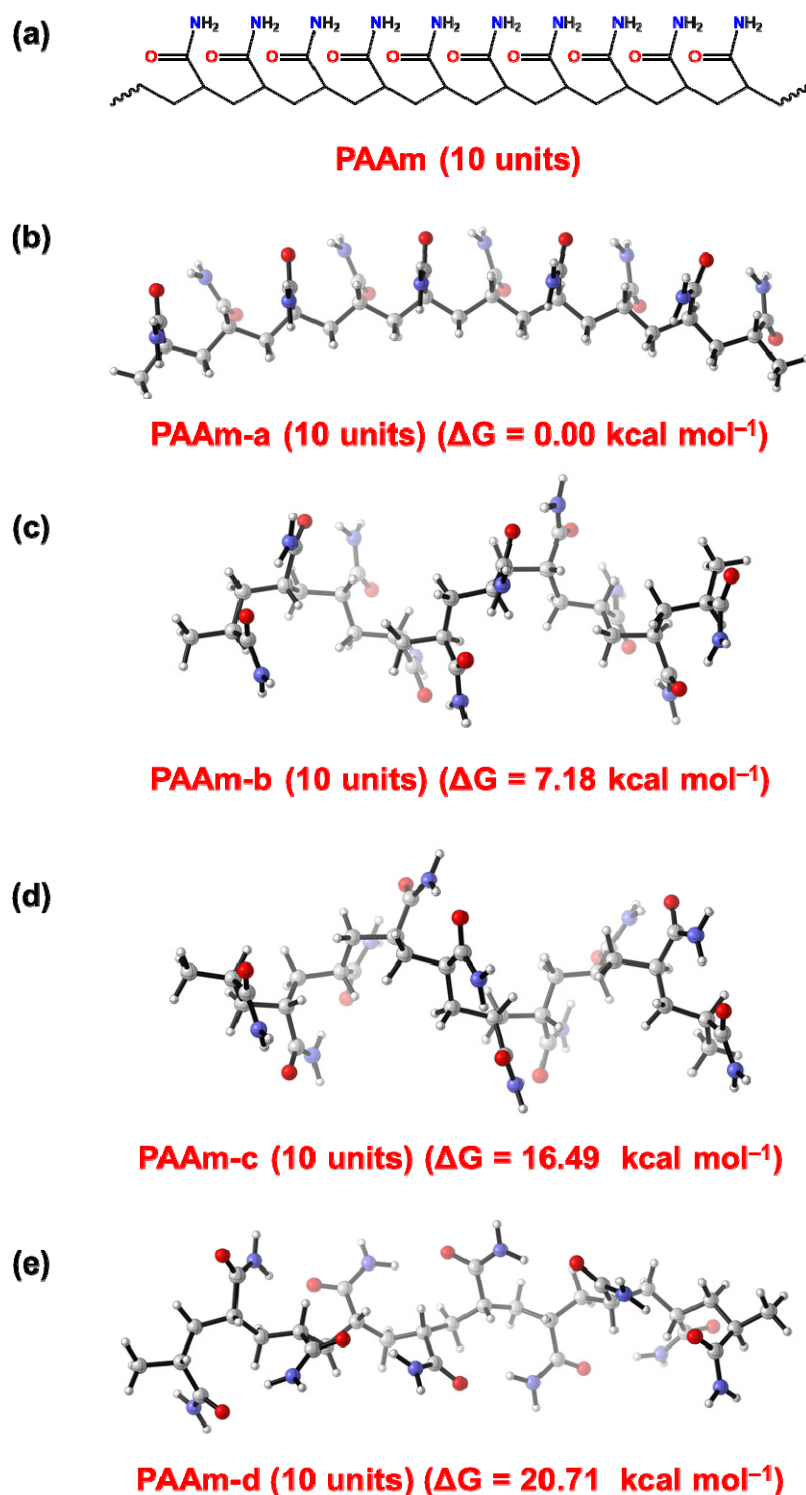
Fig. S6 Computer simulation of PAAm segment (10 units). (a) Chemical structure of PAAm. (b-e) PM7 optimized geometries and calculated relative Gibbs free energy (ΔG) of the four most stable PAAm (10 units) isomers. PAAm-a isomer with the lowest energy was selected to construct the supramolecular-polymer double network in the subsequent calculations.

Table S1. The calculated energies of the species discussed in the main text based on

B3LYP-D3(BJ)/6-31+G(d,p)/SMD(water)//PM7.

Species	Energy (Hartree)
G-CyBA	−1334.698122
(G-CyBA)$_4$-K$^+$	−5938.730084
(G-CyBA)$_{16}$-K$^+$	−23155.393483
PAAm (10 units)	−2514.327988
(G-CyBA)$_{16}$-K$^+$/PAAm (10 units)	−25669.788030

Table S2. The calculated interaction energies based on

B3LYP-D3(BJ)/6-31+G(d,p)/SMD(water)//PM7[a].

Reaction	ΔE_{inter} (kcal mol^{-1})
(G-CyBA)$_{16}$-K$^+$ + PAAm (10 units) → (G-CyBA)$_{16}$-K$^+$/PAAm (10 units)	−41.77

[a] For a given reaction, for example, A + B → complex, the interaction energy is calculated by the following equation: $\Delta E_{inter} = E_{complex} - E_A - E_B$.

Section S3   Mechanical performance of the G-CyBA/PAAm SP-DN hydrogel

Table S3. Effect of G/CyBA/KOH content on the mechanical performance of the G-CyBA/PAAm

SP-DN hydrogels.

	G^a	AAm (g)	MBA^b (μL)	Irgacure 2959 (mg)	Irradiation time (min)	H_2O (mL)	Tensile Fracture stress (MPa)	Tensile Fracture strain (mm mm^{-1})
(G-CyBA)$_x$-AAm$_y$ -MBA$_z$-t	0.0	0.5	46	22.4	30	1.0	0.28	21.7
(G-CyBA)$_x$-AAm$_y$ -MBA$_z$-t	70.0	0.5	46	22.4	30	1.0	0.25	38.6
(G-CyBA)$_x$-AAm$_y$ -MBA$_z$-t	80.0	0.5	46	22.4	30	1.0	0.46	45.6
(G-CyBA)$_x$-AAm$_y$ -MBA$_z$-t	100.0	0.5	46	22.4	30	1.0	0.12	30.1

The compositions of the SP-DN hydrogels were referred as (G-CyBA)$_x$-AAm$_y$-MBA$_z$-t: where x is the mass of G (mg), y is the mass of AAm (g), z is the volume of aqueous MBA (μL), and t is the irradiation time (min) of the UV lamp (365 nm and 0.4 W cm^{-2}). [a]Molar ratio of G:CyBA:KOH was 1:1:1. [b]The concentration of MBA solution was 10 mg mL^{-1}.

Table S4. Effect of AAm content on the mechanical performance of G-CyBA/PAAm SP-DN hydrogels.

	G[a]	AAm (g)	MBA[b] (µL)	Irgacure 2959 (mg)	Irradiation time (min)	H$_2$O (mL)	Tensile Fracture stress (MPa)	Tensile Fracture Strain (mm mm^{-1})
(G-CyBA)$_x$-AAm$_y$ -MBA$_z$-t	80.0	0.3	46	22.4	30	1.0	0.06	12.3
(G-CyBA)$_x$-AAm$_y$ -MBA$_z$-t	80.0	0.4	46	22.4	30	1.0	0.13	27.1
(G-CyBA)$_x$-AAm$_y$ -MBA$_z$-t	80.0	0.5	46	22.4	30	1.0	0.46	45.6
(G-CyBA)$_x$-AAm$_y$ -MBA$_z$-t	80.0	0.6	46	22.4	30	1.0	0.19	25.8

The compositions of the SP-DN hydrogels were referred as (G-CyBA)$_x$-AAm$_y$-MBA$_z$-t: where x is the mass of G (mg), y is the mass of AAm (g), z is the volume of aqueous MBA (µL), and t is the irradiation time (min) of the UV lamp (365 nm and 0.4 W cm^{-2}). [a]Molar ratio of G:CyBA:KOH was 1:1:1. [b]The concentration of MBA solution was 10 mg mL^{-1}.

Table S5. Effect of MBA content on the mechanical performance of the G-CyBA/PAAm SP-DN hydrogels.

	G^a	AAm (g)	MBA^b (μL)	Irgacure 2959 (mg)	Irradiation time (min)	H_2O (mL)	Tensile fracture stress (MPa)	Tensile fracture strain (mm mm^{-1})
$(G-CyBA)_x-AAm_y$ $-MBA_z-t$	80.0	0.5	0	22.4	30	1.0	0.01	0.8
$(G-CyBA)_x-AAm_y$ $-MBA_z-t$	80.0	0.5	23	22.4	30	1.0	0.06	40.3
$(G-CyBA)_x-AAm_y$ $-MBA_z-t$	80.0	0.5	46	22.4	30	1.0	0.46	45.6
$(G-CyBA)_x-AAm_y$ $-MBA_z-t$	80.0	0.5	69	22.4	30	1.0	0.15	18.8

The compositions of the SP-DN hydrogels were referred as $(G-CyBA)_x-AAm_y-MBA_z-t$: where x is the mass of G (mg), y is the mass of AAm (g), z is the volume of aqueous MBA (μL), and t is the irradiation time (min) of the UV lamp (365 nm and 0.4 W cm^{-2}). [a]Molar ratio of G:CyBA:KOH was 1:1:1. [b]The concentration of MBA solution was 10 mg mL^{-1}.

Table S6. Effect of the irradiation time on the mechanical performance of the G-CyBA/PAAm SP-DN hydrogels.

	G^a	AAm (g)	MBA^b (µL)	Irgacure 2959 (mg)	Irradiation time (min)	H_2O (mL)	Tensile fracture stress (MPa)	Tensile fracture strain (mm mm^{-1})
$(G\text{-}CyBA)_x\text{-}AAm_y\text{-}MBA_z\text{-}t$	80.0	0.5	46	22.4	15	1.0	0.11	61.9
$(G\text{-}CyBA)_x\text{-}AAm_y\text{-}MBA_z\text{-}t$	80.0	0.5	46	22.4	20	1.0	0.37	51.9
$(G\text{-}CyBA)_x\text{-}AAm_y\text{-}MBA_z\text{-}t$	80.0	0.5	46	22.4	30	1.0	0.46	45.6
$(G\text{-}CyBA)_x\text{-}AAm_y\text{-}MBA_z\text{-}t$	80.0	0.5	46	22.4	40	1.0	0.34	36.0

The compositions of SP-DN hydrogels were referred as $(G\text{-}CyBA)_x\text{-}AAm_y\text{-}MBA_z\text{-}t$: where x is the mass of G (mg), y is the mass of AAm (g), z is the volume of aqueous MBA (µL), and t is the irradiation time (min) of the UV lamp (365 nm, 0.4 W cm^{-2}). [a]Molar ratio of G:CyBA:KOH was 1:1:1. [b]The concentration of MBA solution was 10 mg mL^{-1}.
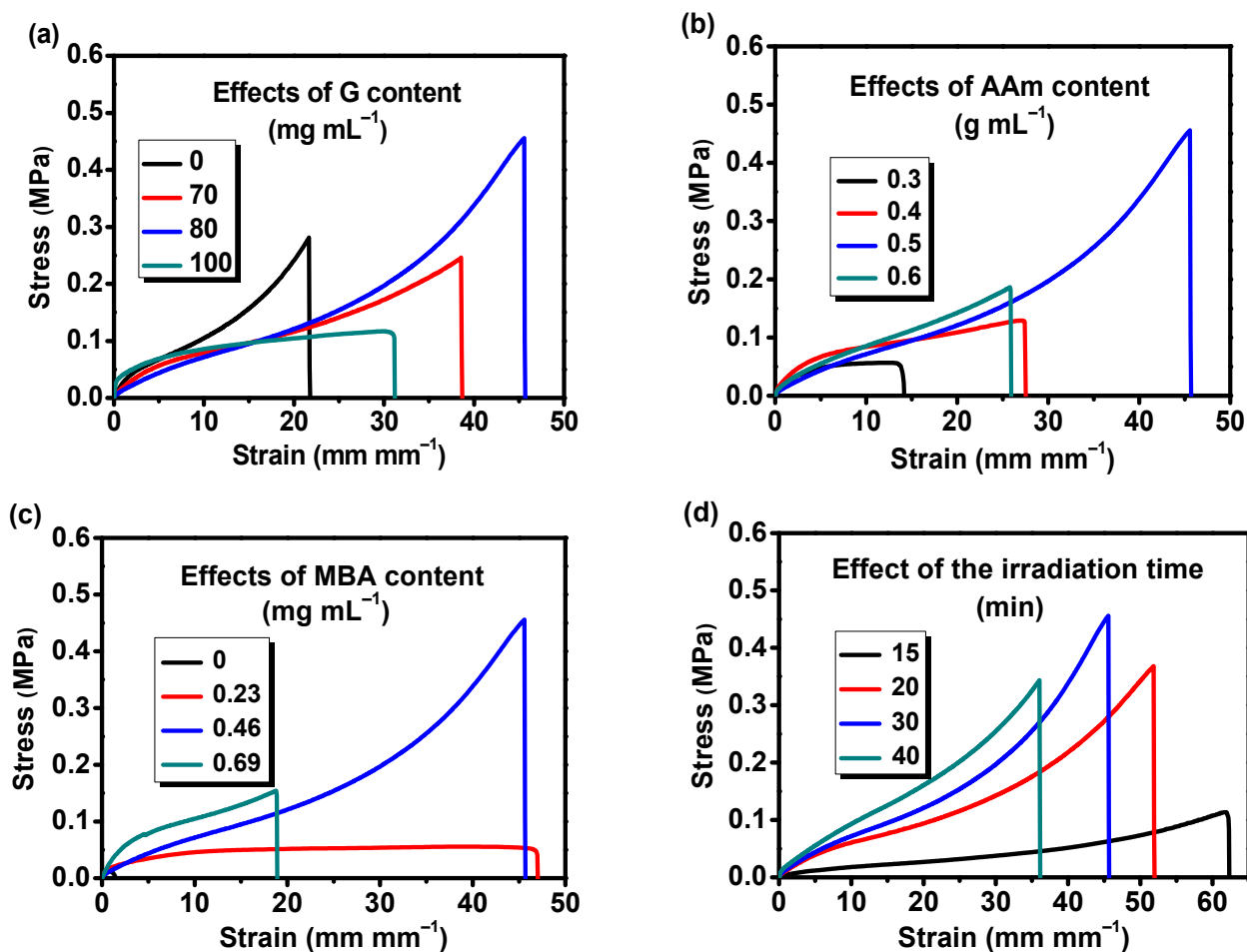
Fig. S7 Optimization of the mechanical properties for G-CyBA/PAAm SP-DN hydrogel. a-d) Tensile stress-strain curves of G-CyBA/PAAm SP-DN hydrogels with varied content of G concentrations (a), AAm concentrations (b), MBA concentrations (c) and Irradiation time of the UV lamp (d).

To construct a SP-DN hydrogel with high mechanical strength and toughness, the effects of G, AAm and MBA concentrations, as well as the irradiation time of the UV lamp on the mechanical properties of the G-CyBA/PAAm SP-DN hydrogel were firstly examined (Tables S3-S6 and Fig. S7). As shown in Fig. S7a, PAAm polymer hydrogel alone showed a tensile fracture strain of 2170%, and fracture stress of 0.28 MPa. Upon introducing of G-CyBA supramolecular network, the mechanical properties of the obtained G-CyBA/PAAm SP-DN hydrogel varied significantly alongwith the G-CyBA concentrations. At G of 80 mg mL^{-1} (molar ratio of G: CyBA was 1:1), the G-CyBA/PAAm SP-DN hydrogel reached the best tensile property (tensile fracture stress of 0.46 MPa; tensile fracture strain of

45.6 mm mm^{-1}), which then drops quickly when excess supramolecular network was incorporated (i.e., G content of 100 mg mL^{-1}). Similarly, without AAm polymer monomers, the G-CyBA supramolecular hydrogel alone was too brittle to bear tensile test. With increasing concentrations of the AAm monomers (from 0.3 to 0.5 g mL^{-1}), the tensile properties of the SP-DN hydrogels increases initially, resulting from the increased density of polymer chains, and then decreases dramatically at a AAm concentration of 0.6 g mL^{-1} probably owing to the broken of the matched balance between the supramolecular and the polymer networks. Without MBA cross-linkers, the as-prepared hydrogel showed negligible stretchability, and the best tensile performance including fracture stress and fracture strain can be achieved at a MAB concentration of 0.46 mg mL^{-1}. Increasing of the UV irradiation time greatly strengthened the SP-DN hydrogels while decreased the stretchability of the hydrogels. To balance the mechanical strength and stretchability, a UV-irradiation time of 30 min was selected to fabricate the robust SP-DN hydrogels. Based on the results mentioned above, unless otherwise stated, the optimal conditions for synthesis of the G-CyBA/PAAm SP-DN hydrogel are G of 80 mg mL^{-1} (molar ratio of G: CyBA was 1:1), AAm of 0.5 g mL^{-1}, MBA of 0.46 mg mL^{-1} and UV-irradiation time of 30 min.
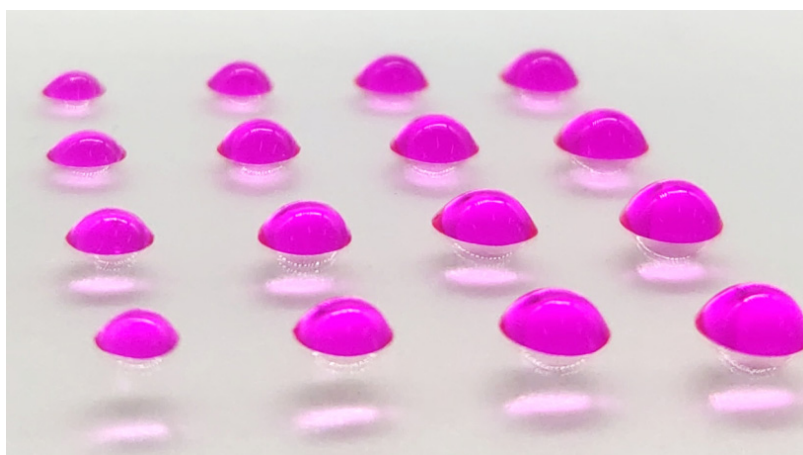
Fig. S8 The injectable capacity of G-CyBA supramolecular hydrogel. The droplets of soft G-CyBA hydrogel were injected by a syringe with increasing sizes and heights. Red dyes of Rhodamine B were added to visually observe the G-CyBA hydrogel.
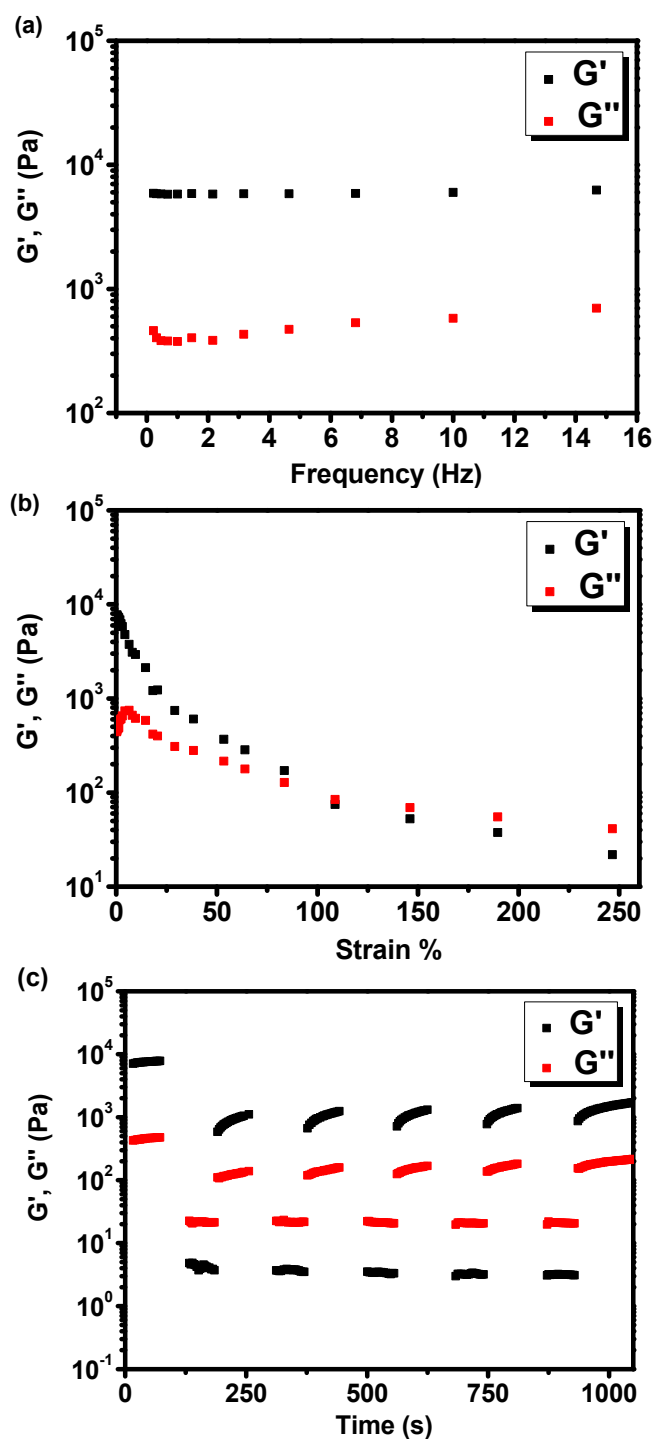
Fig. S9 The mechanical properties of G-CyBA supramolecular hydrogel. a) Dynamic frequency sweep,

b) oscillatory strain sweep and c) step-strain sweep of 3% w/v G-CyBA hydrogel. Rheological test

demonstrated a typical elastic response of the storage modulus (G') and loss modulus (G'') of the

hydrogels, and confirmed the excellent thixotropic property of the hydrogel as G' and G'' could quickly

recover to elastic response of gel during alternative large destructive strain of 100% and a small

recovery strain of 0.1%.

Table S7. Comparison of mechanical properties of the G-CyBA/PAAm SP-DN hydrogel with other DN hydrogels reported in the literature.

Compositions	Tensile fracture stress (MPa)	Tensile fracture strain (mm mm^{-1})	Work of extension at fracture (MJ m^{-3})	*Refs.*
G-CyBA/PAAm SP-DN hydrogel	**0.45**	**45.6**	**7.7**	**This work**
AG/PAAm hydrogel	0.38	21.85	4.4	10
PAAM-PVP hydrogel	0.17	> 180	0.14	11
PAAm/SA/CNT hydrogel	0.03	7.6	–	12
La-cholate/PAAm hydrogel	0.314	29.85	5.678	13
Agar/HPAAm DN hydrogel	0.75	34	–	14
Chitosan/PAM hydrogel	5.6	< 0.45	–	15
Alginate/polyacrylamide hydrogel	0.156	23	–	16
Bulk agar/pHEAA hydrogel	2.6	8	–	17
P(NaSS-co-MPTC) polyampholyte hydrogel	0.1–2.0	1.5–15	0.1–7.0	18
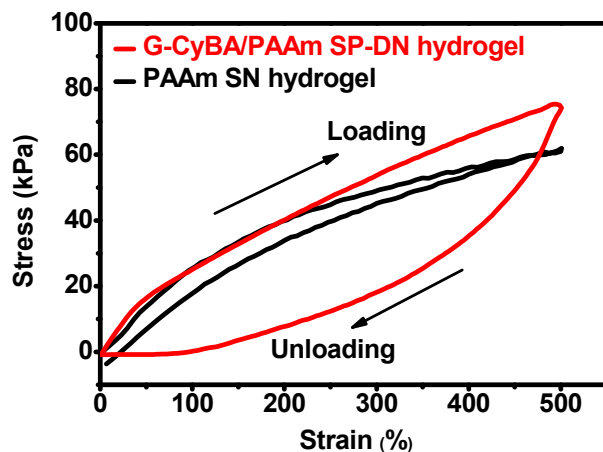
Fig. S10 The loading-unloading curves of the SP-DN and the PAAm SN hydrogels

at the tension strain of 500%.
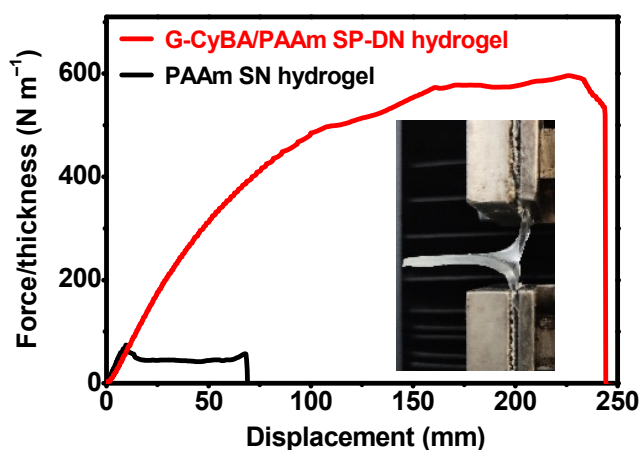
Fig. S11 Tearing curves of the PAAm SN and the G-CyBA/PAAm SP-DN hydrogels, showing an

improved tearing energy of up to ~1160 J m^{-2}, remarkably outperforming that of the PAAm polymer

SN hydrogel (~88 J m^{-2}).
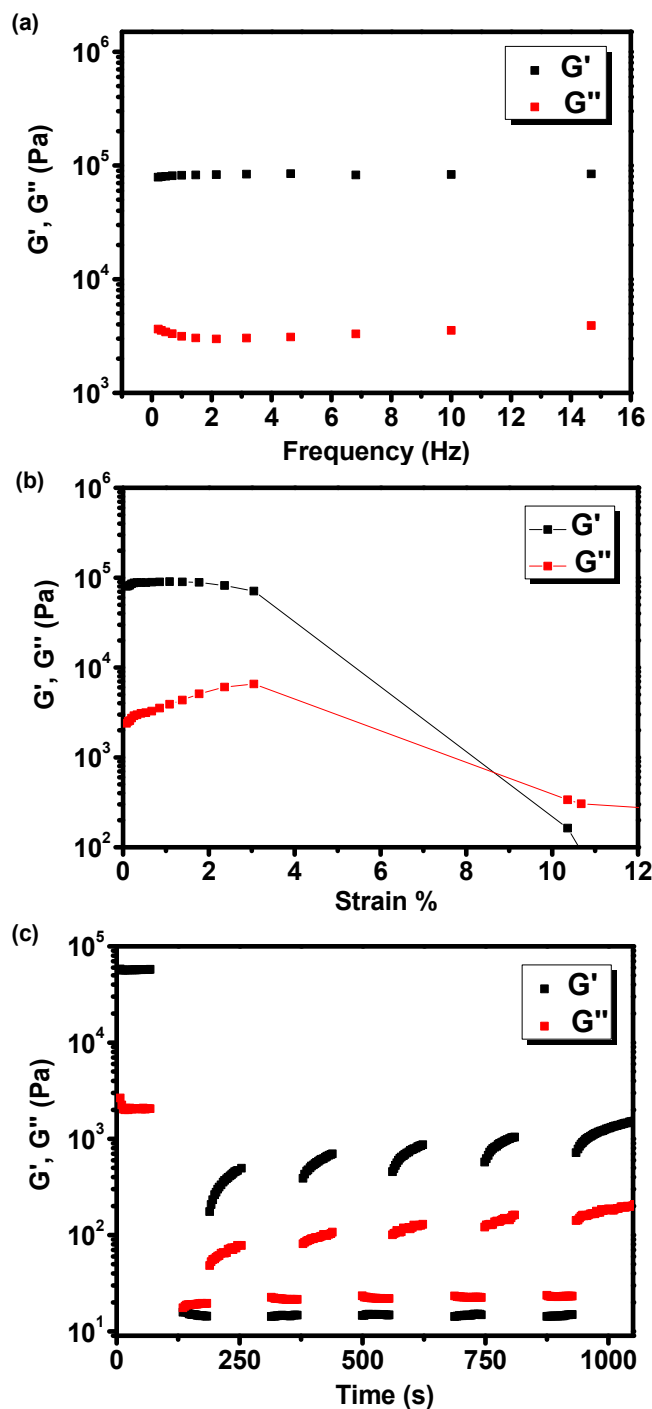
Fig. S12 The mechanical properties of guanosine-boric acid (G-BA) hydrogels. (a) Dynamic frequency sweep, (b) oscillatory strain sweep and (c) step-strain sweep of 3% w/v G-BA supramolecular hydrogels. Rheological test demonstrated a typical elastic response of the storage modulus (G') and loss modulus (G'') of the hydrogels, and confirmed the excellent thixotropic property of the hydrogels as G' and G'' could quickly recover to elastic response of the gels during alternative large destructive strain of 100% and a small recovery strain of 0.1%.

26
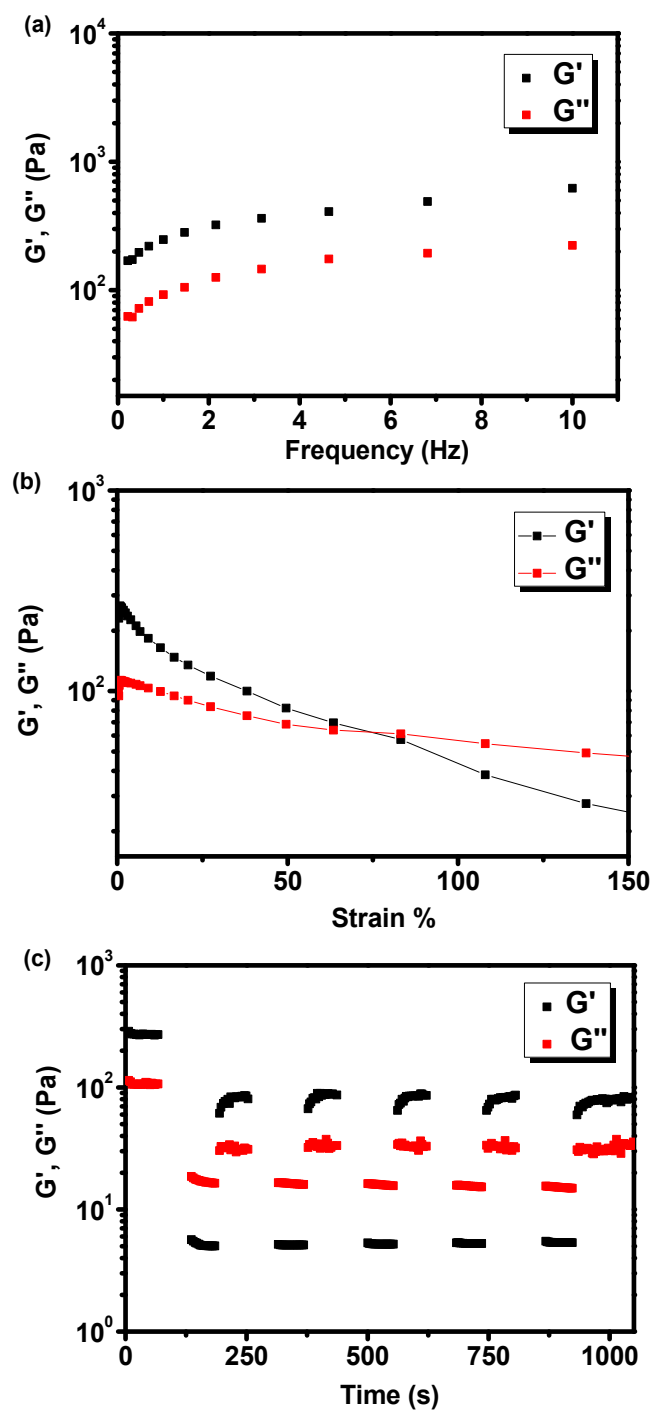
Fig. S13 The mechanical properties of guanosine-phenylboronic acid (G-PBA) supramolecular hydrogels. (a) Dynamic frequency sweep, (b) oscillatory strain sweep and (c) step-strain sweep of 3% w/v G-PBA hydrogels. Rheological test demonstrated a typical elastic response of the storage modulus (G') and loss modulus (G'') of the hydrogels, and confirmed the excellent thixotropic property of the hydrogel as G' and G'' could quickly recover to elastic response of the gels during alternative large destructive strain of 100% and a small recovery strain of 0.1%.

27
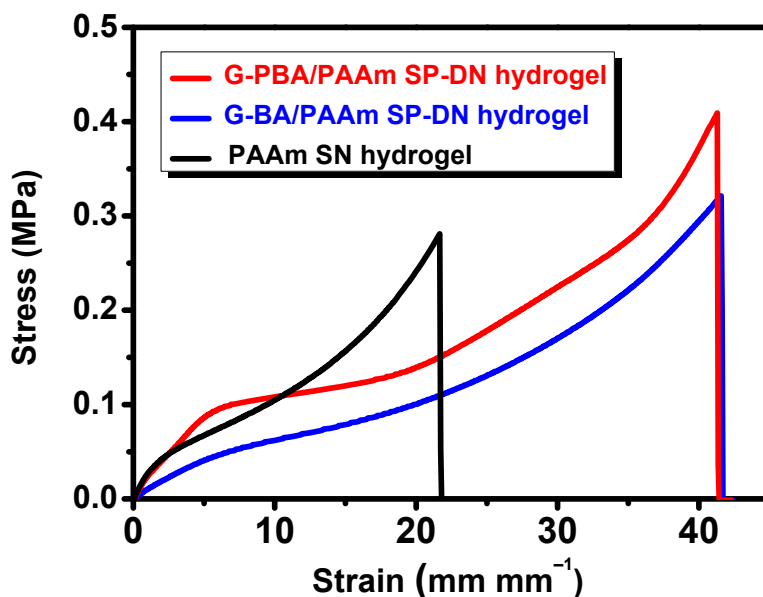
Fig. S14 Tensile properties of the SP-DN hydrogels and the PAAm SN hydrogel. Tensile stress-strain curves of the PAAm SN hydrogel and G-PBA/PAAm and G-BA/PAAm SP-DN hydrogels, showing the enhanced tensile fracture strain and the fracture stress of the SP-DN hydrogels by introducing G-PBA or G-BA supramolecular network.
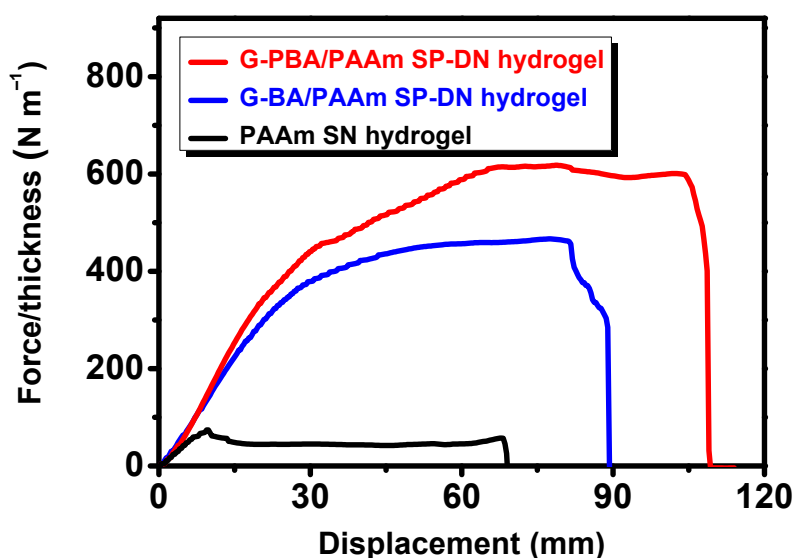
Fig. S15 Toughness of the SP-DN hydrogels and PAAm SN hydrogelQ determined by tearing test. Tearing curves of the PAAm SN hydrogel, G-PBA/PAAm and G-BA/PAAm SP-DN hydrogels, displaying significantly improved tearing energy of the SP-DN hydrogels by introducing G-PBA or G-BA supramolecular network.

Section S4   Mechanical performance and conductivity of KOH-filled G-CyBA/PAAm SP-DN hydrogel
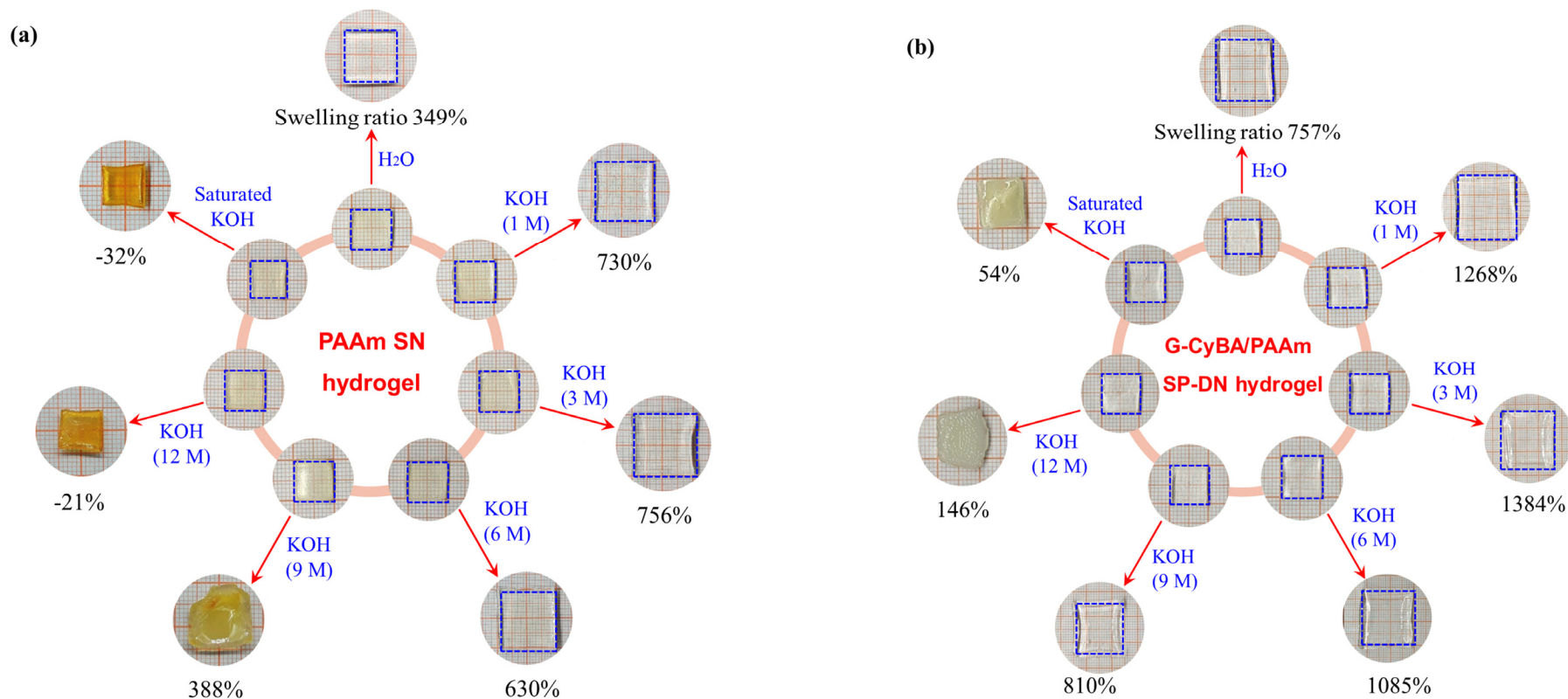
Fig. S16 Swelling performance of the PAAm SN and the G-CyBA/PAAm SP-DN hydrogels in various concentrations of aqueous KOH. a-b) Experimental photos and swelling ratios of the PAAm SN hydrogel (a) and the G-CyBA/PAAm SP-DN hydrogel (b) at the initial and swelling equilibrium state, demonstrating the dramatically improved KOH (aq.) absorption capacity of the SP-DN hydrogel by introducing G-CyBA supramolecular network.
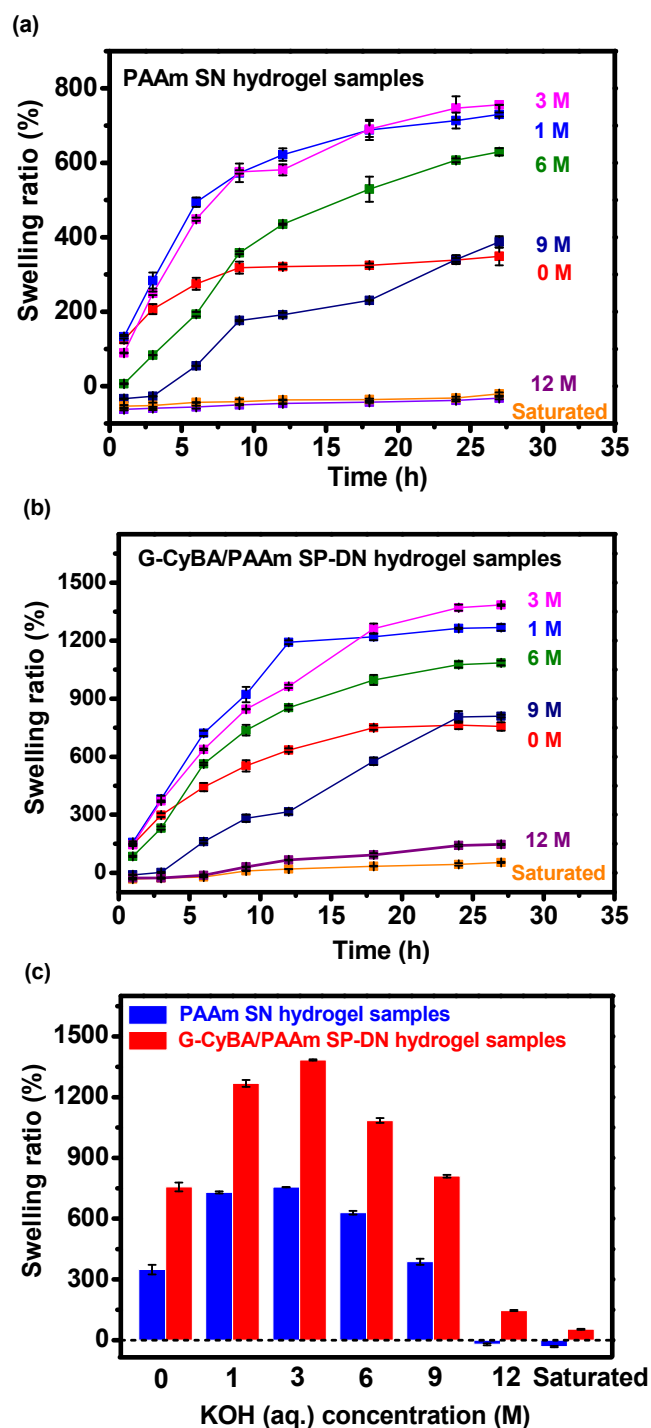
Fig. S17 Swelling dynamics of the PAAm SN and the G-CyBA/PAAm SP-DN hydrogels in different

concentrations of aqueous KOH. The swelling ratios of a) the PAAm SN hydrogel samples and b) the

G-CyBA/PAAm SP-DN hydrogel samples along with varying soaking time in various concentrations of

aqueous KOH. c) Comparison of the swelling ratios between the PAAm SN and the G-CyBA/PAAm

SP-DN hydrogel samples after swelling equilibrium in different concentrations of aqueous KOH. Error

bars represent standard deviations of data collected from at least three separate samples.
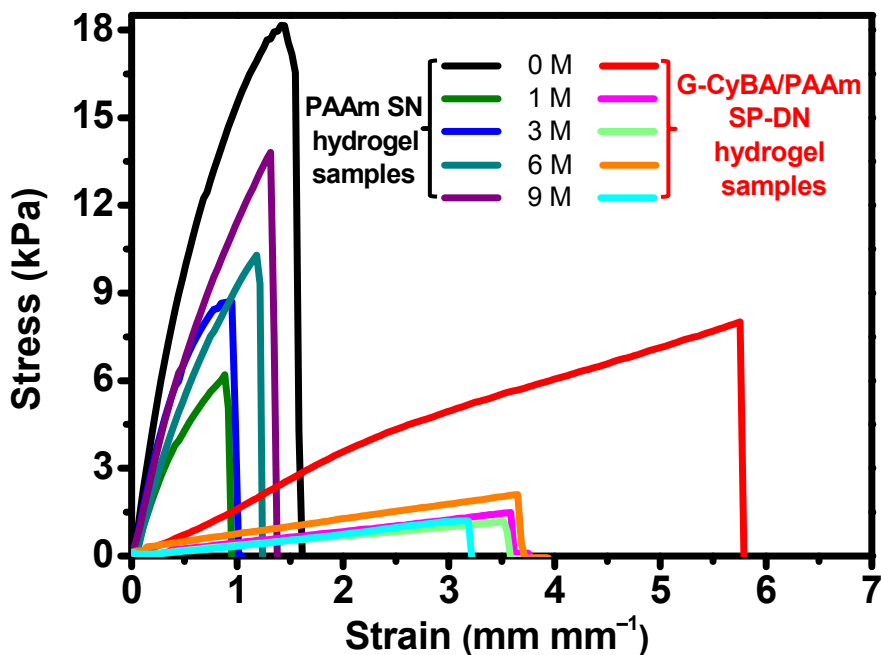
Fig. S18 Tensile properties of the PAAm SN and G-CyBA/PAAm SP-DN hydrogel samples after swelling equilibrium in different concentrations of aqueous KOH. Tensile stress-strain curves of the hydrogel samples, suggesting a better stretchability of the KOH (0–9 M)-filled SP-DN hydrogels by introducing G-CyBA supramolecular network.

31
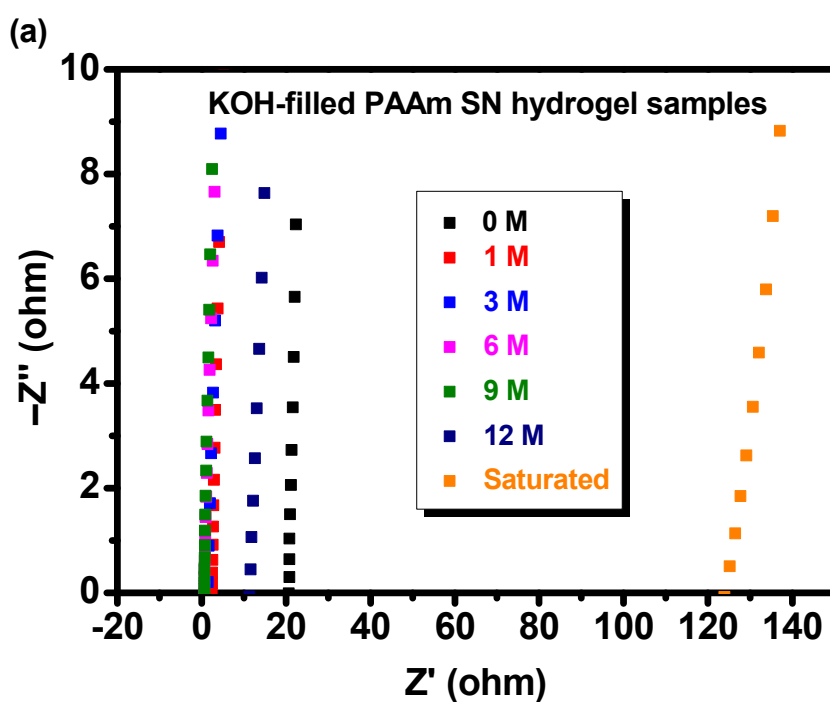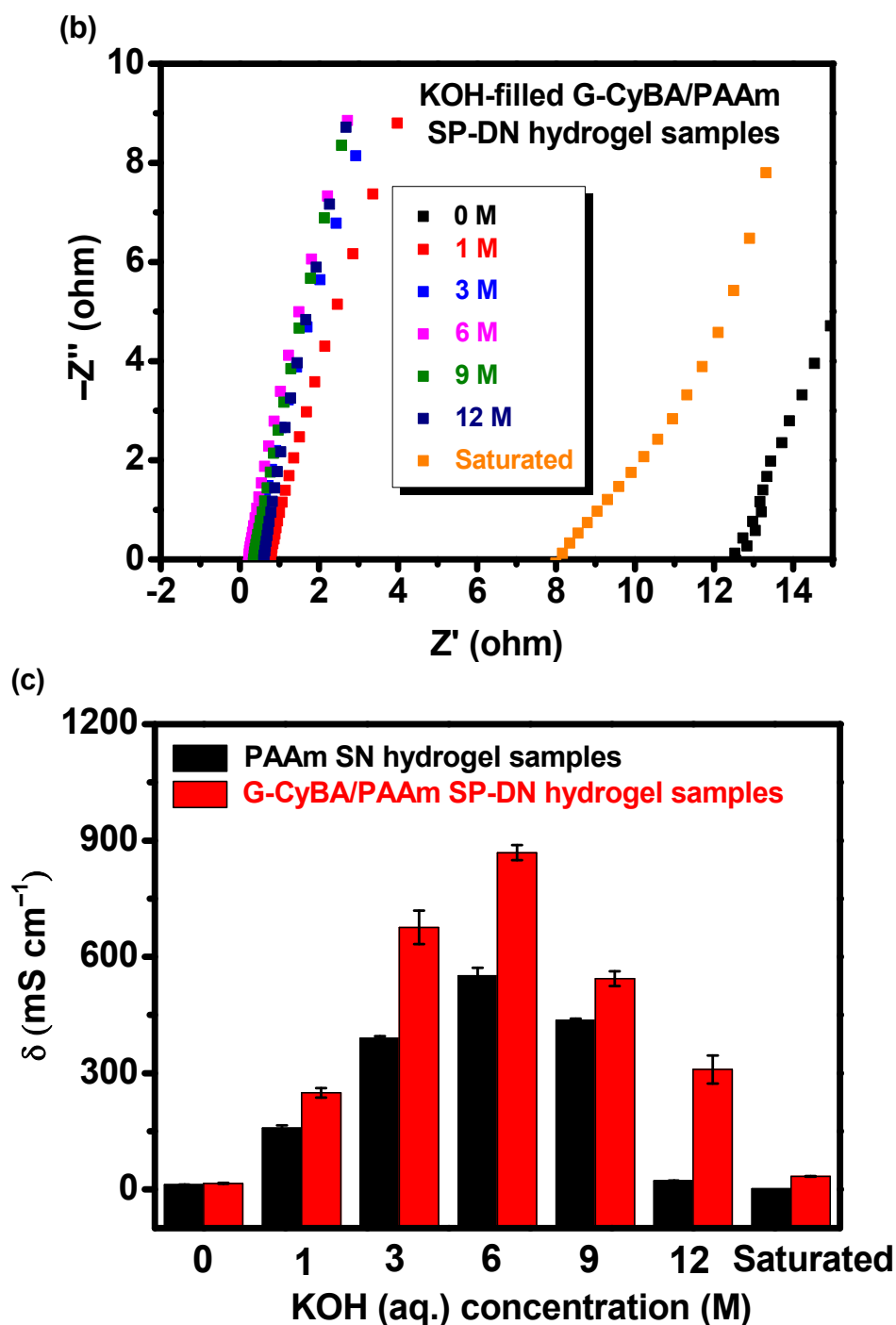
Fig. S19 Ionic conductivity of the KOH-filled PAAm SN and the KOH-filled G-CyBA/PAAm SP-DN hydrogel samples after swelling equilibrium. (a) The EIS plot of the KOH-filled PAAm SN hydrogel samples, (b) the KOH-filled G-CyBA/PAAm SP-DN hydrogel samples and (c) their corresponding ionic conductivity calculated from the EIS plot, showing a improved conductivity of the KOH-filled SP-DN hydrogels by introducing G-CyBA supramolecular network. Error bars represent standard deviations of data collected from at least three separate samples.

(a)

(b)

(c)
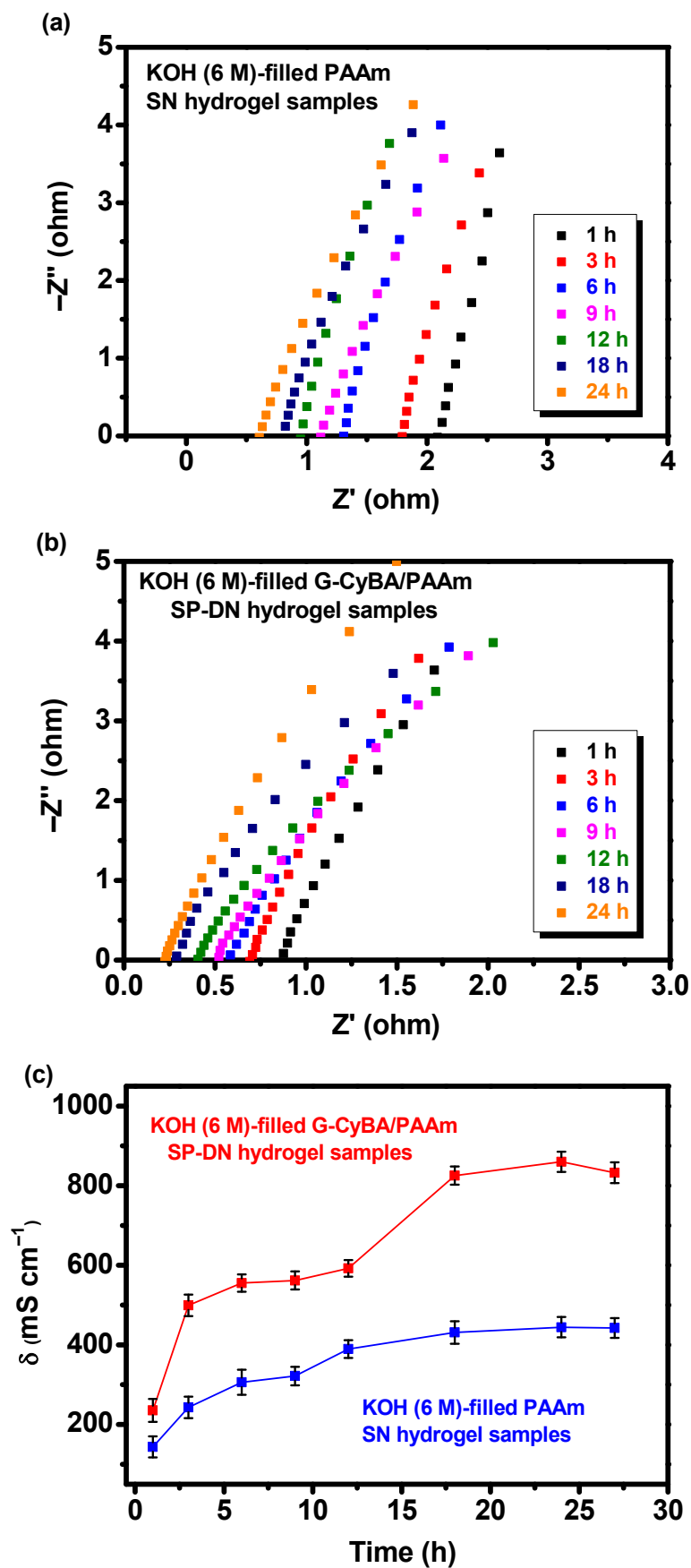
Fig. S20 Ionic conductivity of the KOH (6 M)-filled PAAm SN and G-CyBA/PAAm SP-DN hydrogel samples along with varying soaking time. The EIS plot of (a) the KOH (6 M)-filled PAAm SN hydrogel samples, (b) the KOH (6 M)-filled G-CyBA/PAAm SP-DN hydrogel samples and (c) their corresponding ionic conductivity calculated from the EIS plot at different soaking time, showing an ultra-high conductivity of the KOH-filled SP-DN hydrogels by introducing G-CyBA supramolecular network. Error bars represent standard deviations of data collected from at least three separate samples.
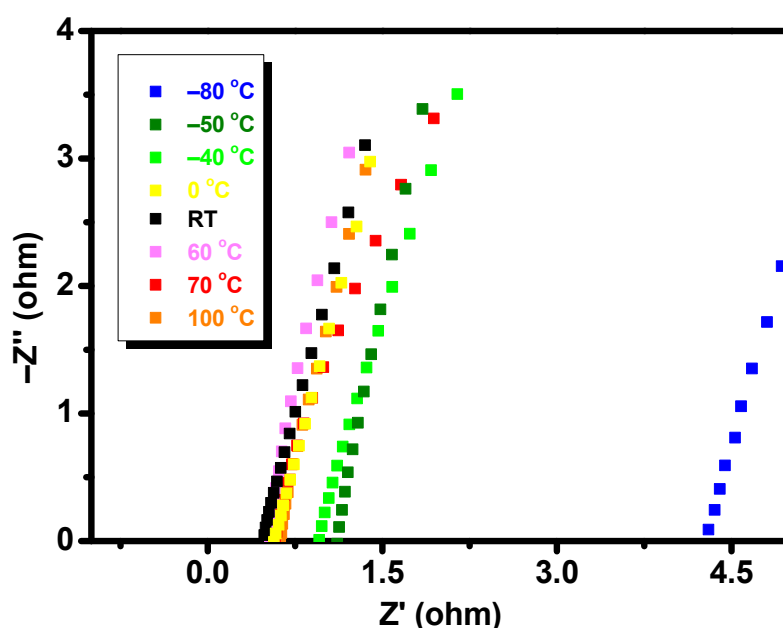
Fig. S21 EIS plot of the KOH (6 M)-filled G-CyBA/PAAm SP-DN hydrogel samples with 600% swelling ratio at various temperatures.

Table S8. Comparison of the 600%-KOH (6 M)-filled G-CyBA/PAAm SP–DN hydrogel in this work with previous reported anti-freezing hydrogels in terms of ionic conductivity, working temperatures and mechanical properties.

Gel network	Deicing agents	Work temperature range	Ionic conductivity (mS cm^{-1})	Stretchability at RT	*Refs.*
G-CyBA/PAAm	KOH	–80 to 100 °C	431.7 (100 °C) 486.0 (70 °C) 519.9 (60 °C) 571.1 (25 °C) 487.7 (0 °C) 300.1 (–40 °C) 252.2 (–50 °C) 63.2 (–80 °C)	1626%	This work
PVAA–GO	KI/KOH	RT	155 (RT)	_	19
PANa-cellulose	KOH	RT	280 (RT)	> 1000%	20
PAM	LiCl	RT	120 (RT)	_	21
PAA	KOH	–20 to 25 °C	275 (25 °C) 199 (–20 °C)	680%	22
PAMPS-K25 -MC2.0	KOH	–20 °C to RT	105 (RT) 18.1 (–20 °C)	162%	23
P(AM-co-AA)/CS	Fe(NO$_3$)$_3$·9H$_2$O Na$_2$SO$_4$	–30 °C to RT	30.4 (RT)	1225%	24
PANa	KOH	–20 to 50 °C	163 (50 °C) 126 (24 °C) 57 (–20 °C)	1400%	25
PAAm/PAA /Fe^{3+}	NaCl	–24.7 to 60 °C	7.2 (25 °C)	573.5%	26

(Continued)

Gel network	Deicing agents	Work temperature range	Ionic conductivity (mS cm^{-1})	Stretchability at RT	*Refs.*
PAAm-alginate	CaCl$_2$	−70 to 25 °C	~80 (25 °C) ~50 (0 °C) ~40 (−15 °C) ~18 (−30 °C) ~2 (−50 °C)	500%	27
Cellulose	ZnCl$_2$/CaCl$_2$	−70 to 25 °C	74.9 (25 °C)	100%	28
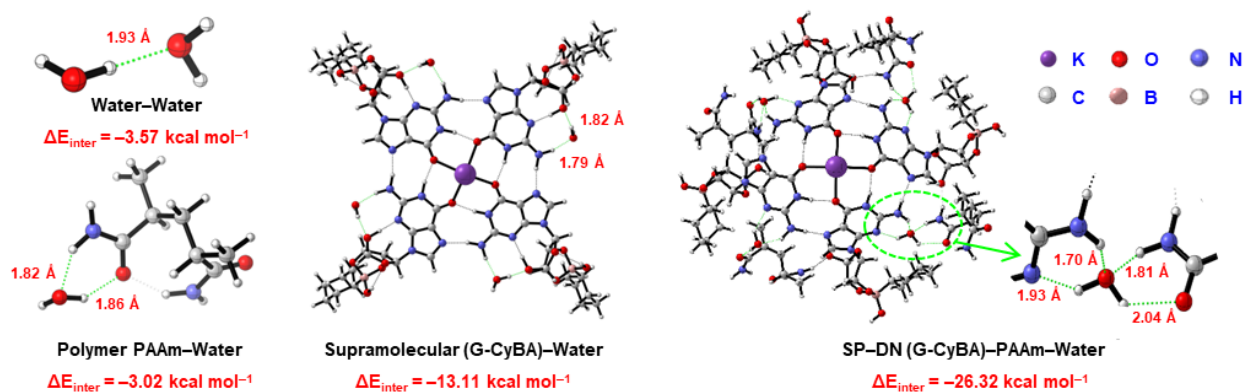
Fig. S22 Simulated interactions between water and building blocks of the G-CyBA supramolecular

network, the PAAm polymer network, and the G-CyBA/PAAm supramolecular-polymer double

network.

Table S9. The calculated energies of the species discussed in the main text based on B3LYP-D3(BJ)/6-31+G(d,p)/SMD(water)//PM7.

Species	Energy (Hartree)
$(G\text{-}CyBA)_4\text{-}K^+$	−5938.730084
PAAm (2 units)	−535.282896
H_2O	−76.448343
$H_2O\text{−}H_2O$	−152.902369
PAAm (2 units)/H_2O	−611.736044
$(G\text{-}CyBA)_4\text{-}K^+/4H_2O$	−6244.544349
$(G\text{-}CyBA)_4\text{-}K^+/4PAAm$ (2 units)/$4H_2O$	−8385.696986

Table S10. The calculated interaction energies based on

B3LYP-D3(BJ)/6-31+G(d,p)/SMD(water)//PM7[a].

Reactions	ΔE_{inter} (kcal mol^{-1})
$H_2O + H_2O \rightarrow H_2O/H_2O$	-3.57
PAAm (2 units) + $H_2O \rightarrow$ PAAm (2 units)/H_2O	-3.02
(G-CyBA)$_4$-K$^+$ + 4 $H_2O \rightarrow$ (G-CyBA)$_4$-K$^+$/4 H_2O	-13.11
(G-CyBA)$_4$-K$^+$ + 4 PAAm (2 units) + 4$H_2O \rightarrow$ (G-CyBA)$_4$-K$^+$/4 PAAm (2 units)/4 H_2O	-26.32

[a] For a given reaction, for example, A + B $\rightarrow$ complex, the interaction energy is calculated by the following equation: $\Delta E_{inter} = E_{complex} - E_A - E_B$.

Section S5   Adhesiveness of 600%-KOH (6 M)-filled G-CyBA/PAAm SP-DN hydrogel
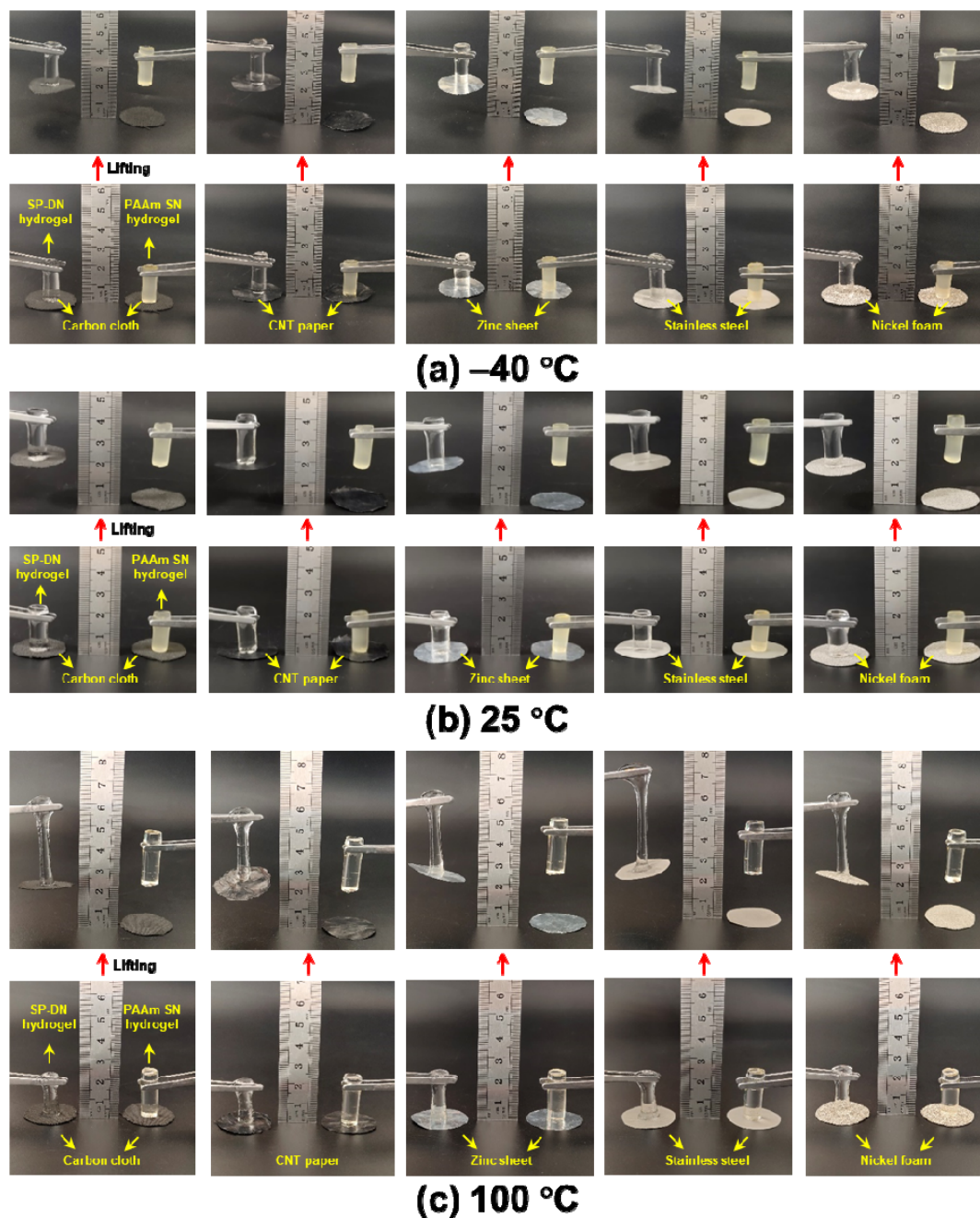
Fig. S23 Comparison of the adhesiveness under (a) –40 °C, (b) 25 °C and 9c) 100 °C between the 600%-KOH (6 M)-filled G-CyBA/PAAm SP-DN hydrogel and the KOH (6 M)-filled PAAm SN hydrogel counterparts. Various electrode substrates, such as carbon cloth, CNT paper, zinc sheet, stainless steel mesh, and nickel foam could be readily lifted *via* the adhesion of the 600%-KOH (6 M)-filled SP-DN hydrogel without using any adhesive or surface treatment, while KOH (6 M)-filled PAAm SN hydrogel, whether fully swollen or not, failed to adhere any of the above electrode materials.
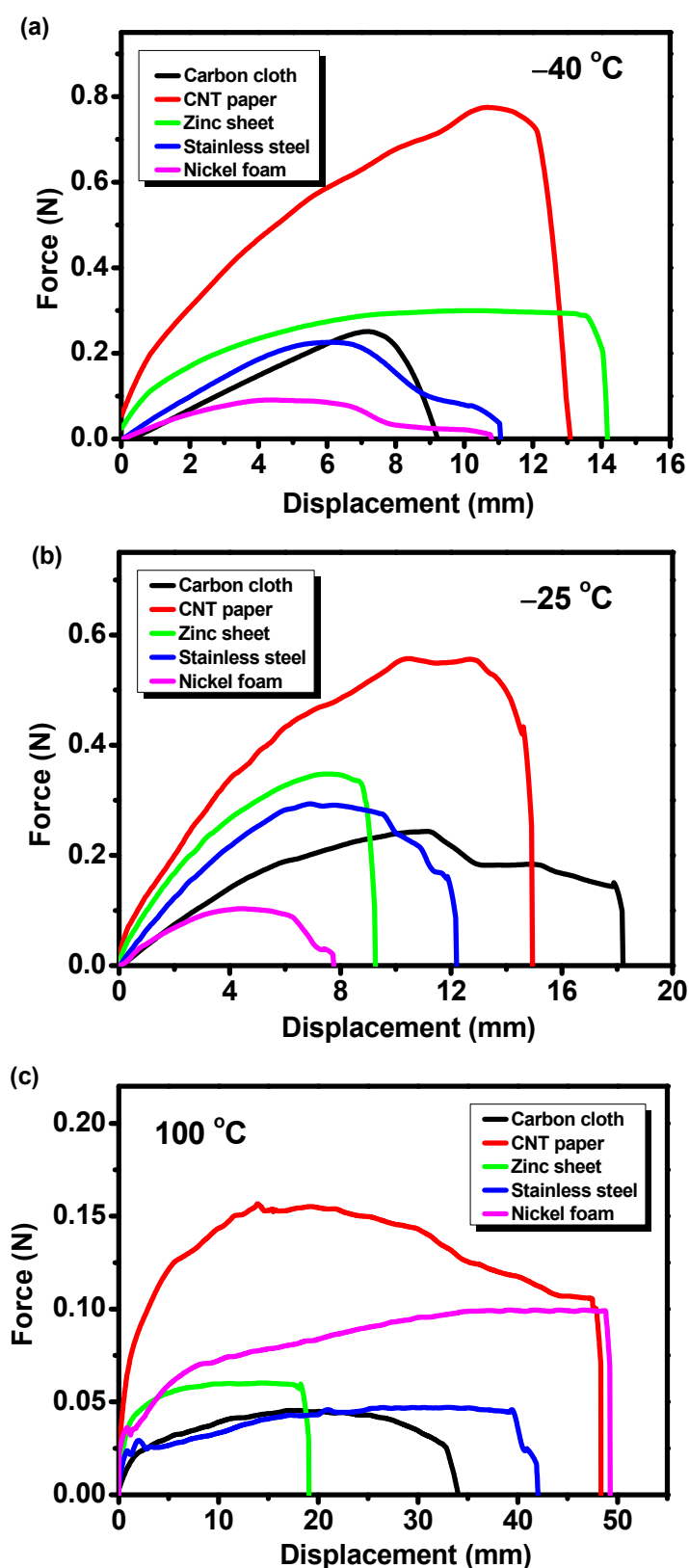
Fig. S24 Lap-shear test of the 600%-KOH (6 M)-filled G-CyBA/PAAm SP-DN hydrogel to various electrode substrates under a) –40 ºC, b) 25 ºC and c) 100 ºC, respectively.

Section S6 Electrochemical performance of the Zn–air battery based on 600%-KOH (6 M)-filled G-CyBA/PAAm SP-DN hydrogel electrolyte

(a)

Wrapping zinc spring using 600%-KOH (6 M)-filled SP-DN hydrogel

Further wrapping using CNT paper loaded with catalyst

Flexible Zn–air battery wrapped by a heat shrinkable tube

(b)

Wrapping zinc spring using 600%-KOH (6 M)-filled SP-DN hydrogel

Pre-stretching

Further wrapping using CNT paper loaded with catalyst

Releasing to obtain the final stretchable Zn–air battery
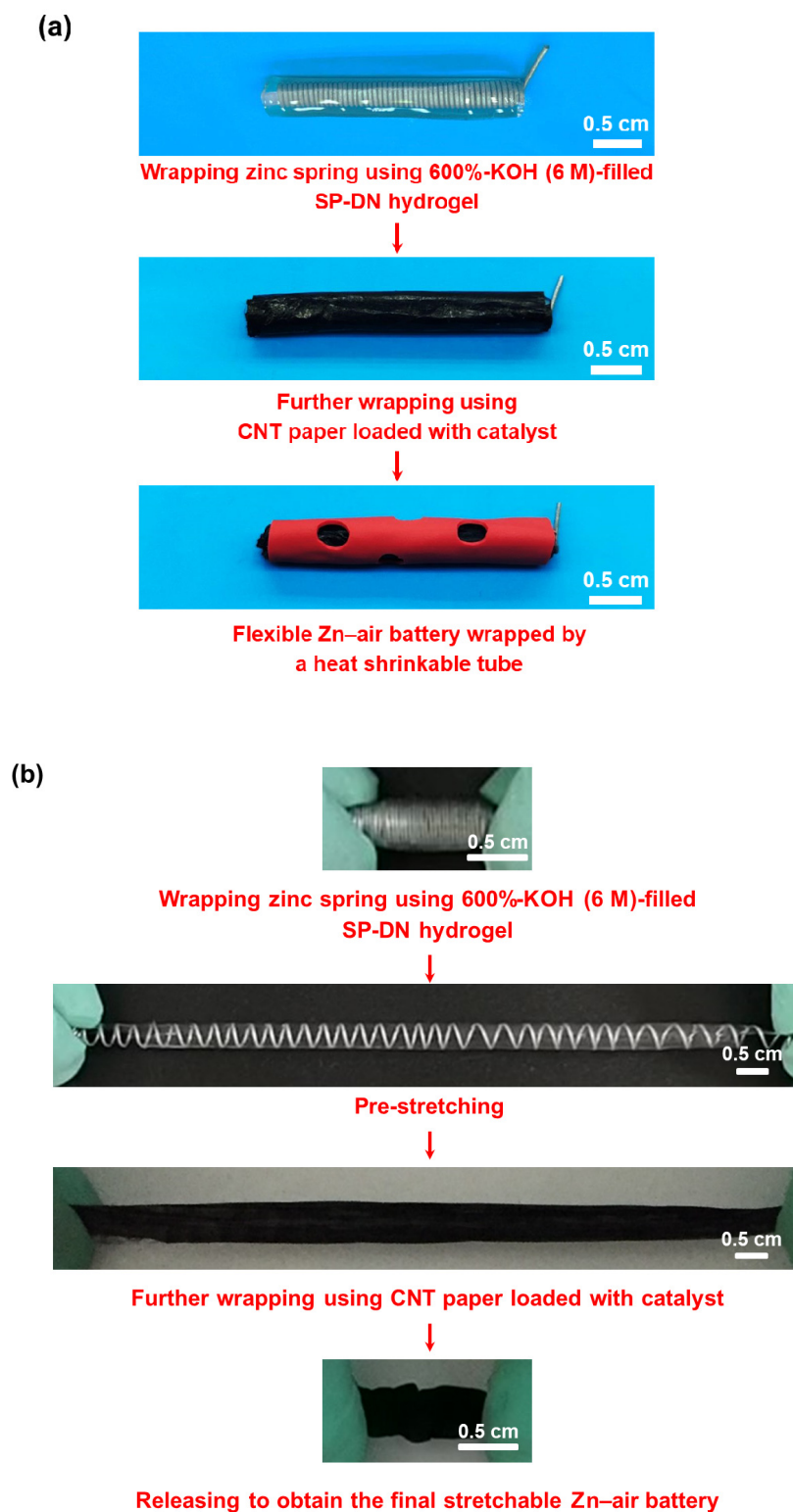
Fig. S25 The manufacturing process of (a) the flexible Zn–air battery and (b) the stretchable Zn–air battery based on the 600%-KOH (6 M)-filled SP-DN hydrogel electrolyte.
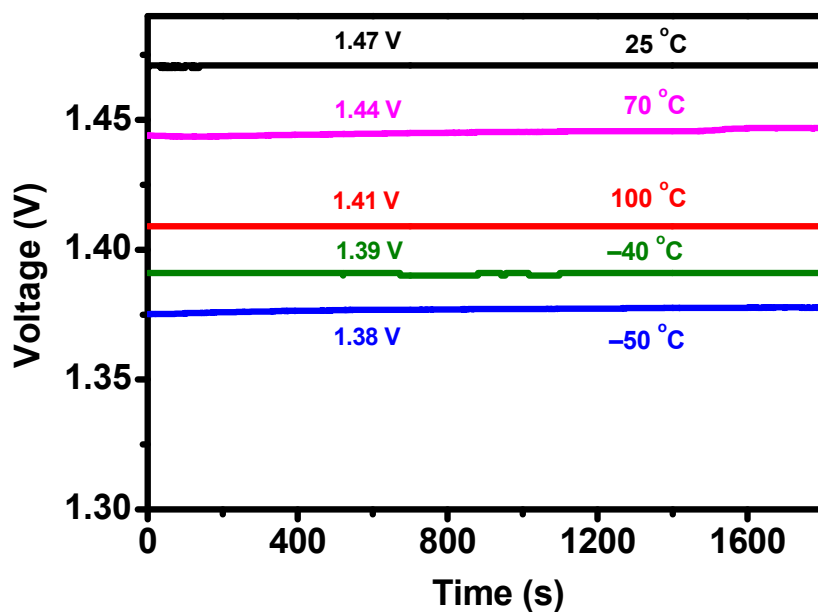
Fig. S26 Temperature-dependent performances of the ZAB. Open-circuit voltages of the ZAB at 100, 70, 25, –40, and –50 °C.
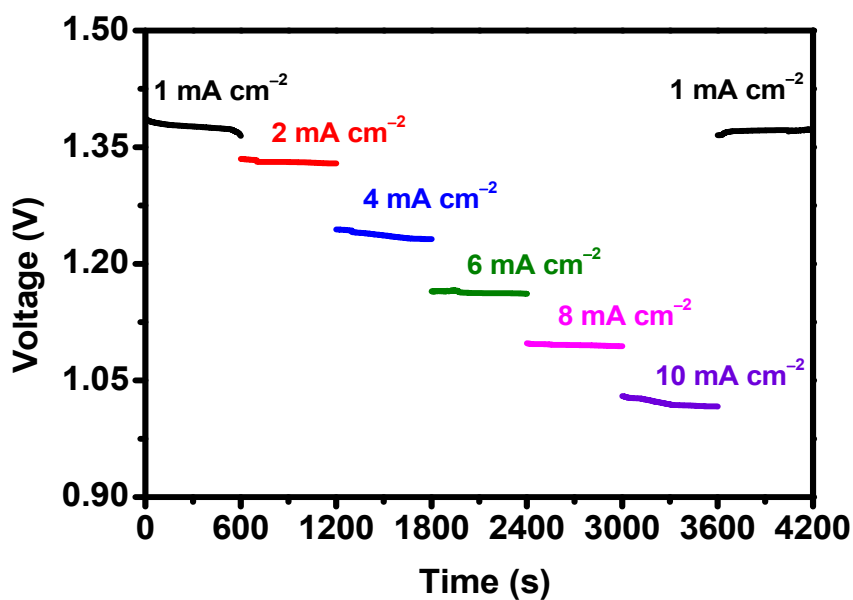
Fig. S27 Rate discharge properties of the ZAB. Discharging plateaus of the ZAB at different current densities, suggesting excellent rate discharge performance and resilience capability.
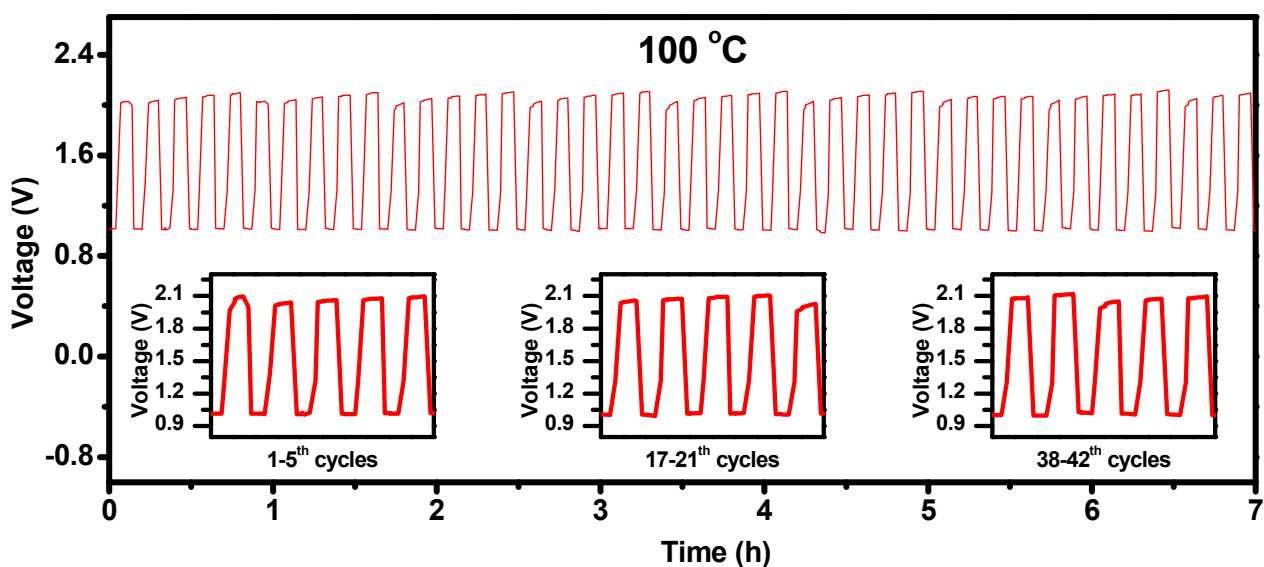
Fig. S28 Cycling stability of the ZAB at 100 °C. Galvanostatic discharge and charge curves of the ZAB. Inset: magnified plots of the galvanostatic discharge and charge curves at different cycles. The results showed that the ZAB can be stably charged and discharged up to 42 cycles for 7 h at 100 °C under a current density of 2 mA cm^{-2}.
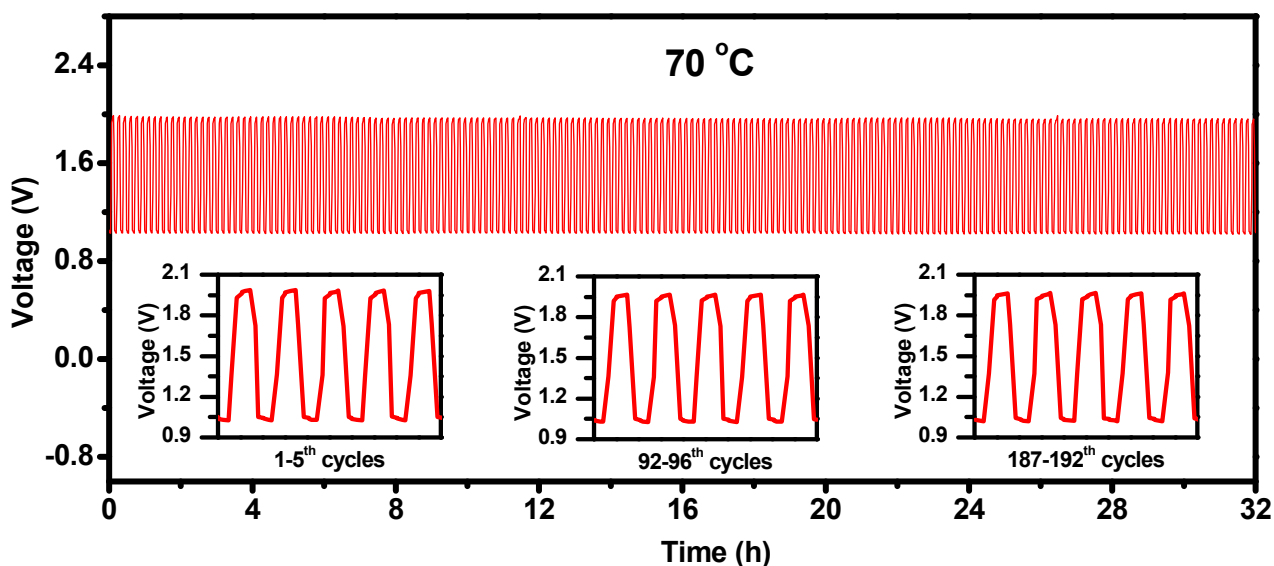
Fig. S29 Cycling stability of the ZAB at 70 °C. Galvanostatic discharge and charge curves of the ZAB. Inset: magnified plots of the galvanostatic discharge and charge curves at different cycles. The results showed that the ZAB can be stably charged and discharged up to 192 cycles for 32 h at 70 °C under a current density of 2 mA cm^{-2}.
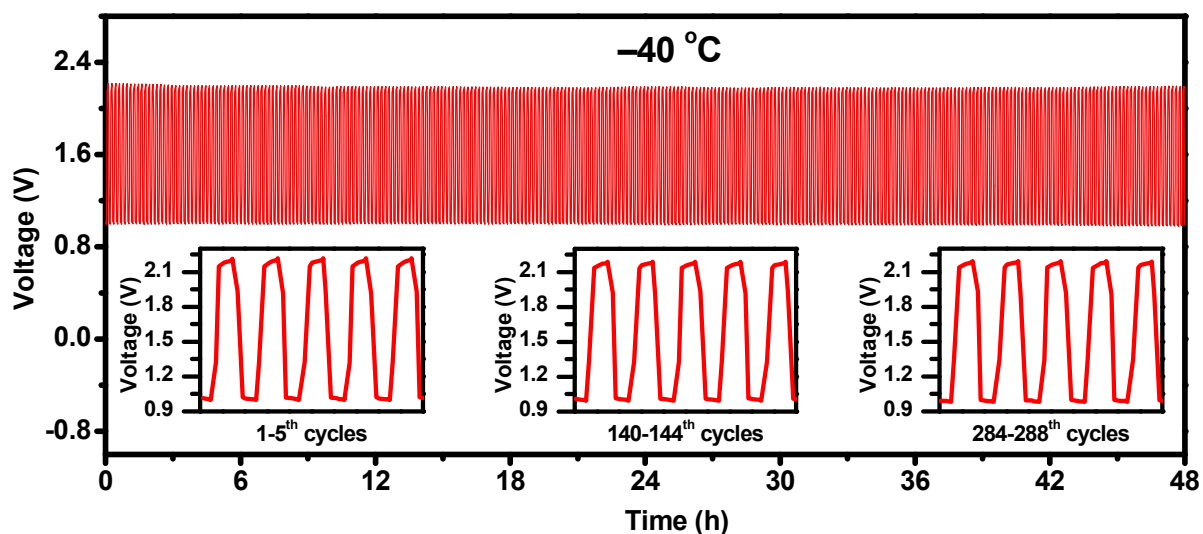
Fig. S30 Cycling stability of the ZAB at –40 °C. Galvanostatic discharge and charge curves of the ZAB. Inset: magnified plots of the galvanostatic discharge and charge curves at different cycles. The results showed that the ZAB can be stably charged and discharged up to 288 cycles for 48 h at –40 °C under a current density of 2 mA cm^{-2}.
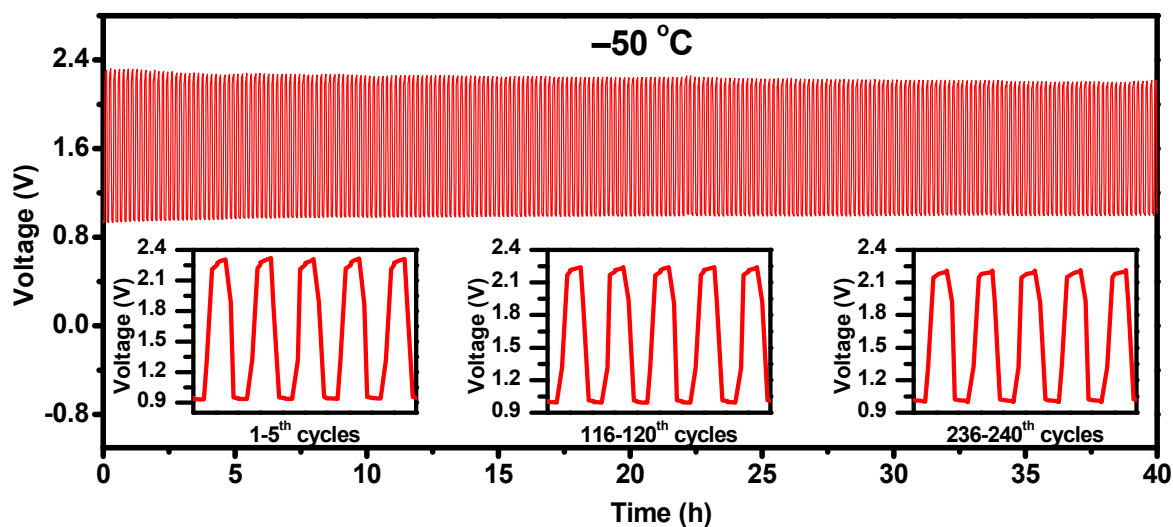
Fig. 31 Cycling stability of the ZAB at –50 °C. Galvanostatic discharge and charge curves of the ZAB. Insets: magnified plots of the galvanostatic discharge and charge curves at different cycles. The results showed that the ZAB can be stably charged and discharged up to 240 cycles for 40 h at –50 °C under a current density of 2 mA cm^{-2}.
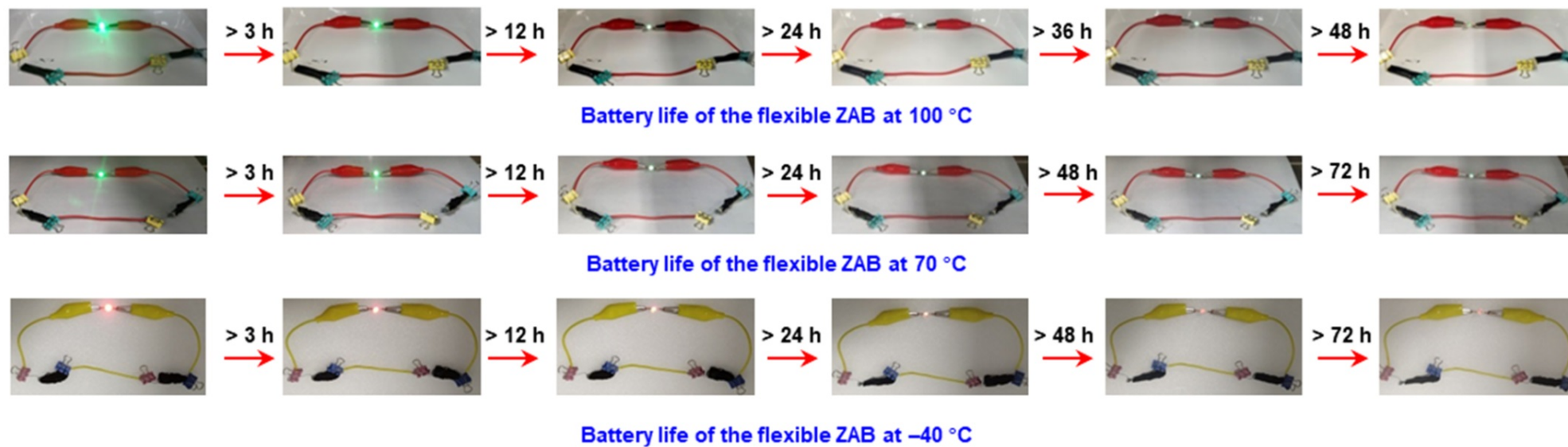
Fig. S32 Battery life of the flexible ZABs at various temperatures, which can continuously power a LED for over 48 h (100 °C)

and over 72 h (70 °C and −40 °C).
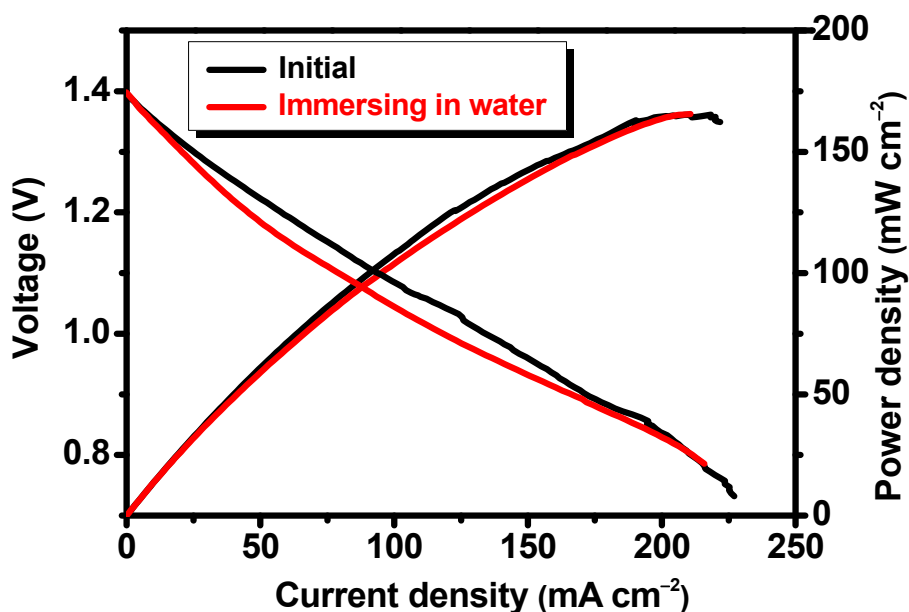
Fig. S33 Waterproof performance of the ZAB. Discharge profiles and the corresponding power density curves of the ZAB immersed in water *in situ*, showing comparable electrochemical performance after 2 h of immersing as that of the initial.
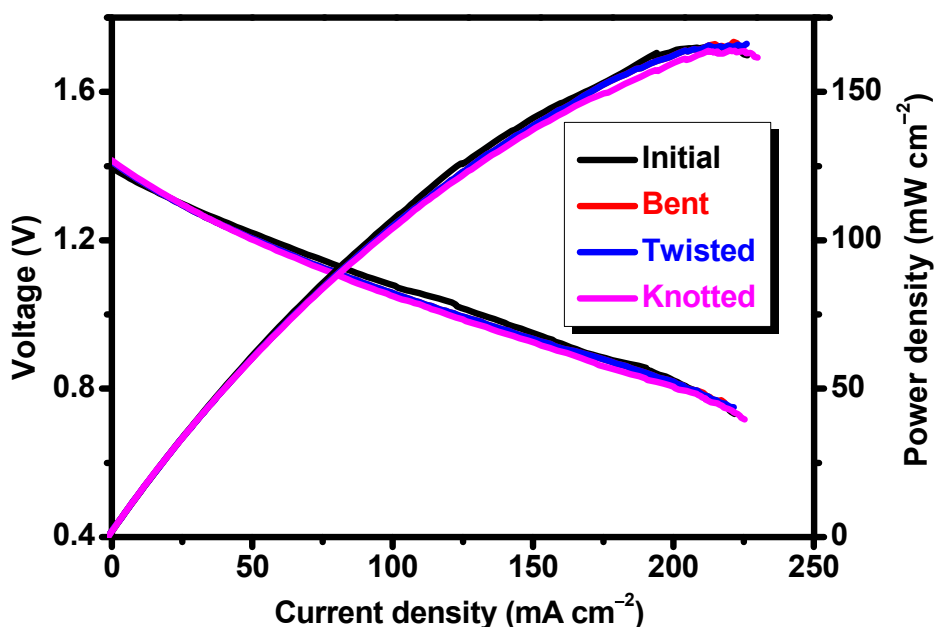
Fig. S34 Mechanical and electrochemical robustness of the flexible ZAB.Discharge profiles and the corresponding power density curves of the ZAB under diversiform deformations, which presents very stable power density and charge-discharge profiles when subject to bending, twisting, and knotting.
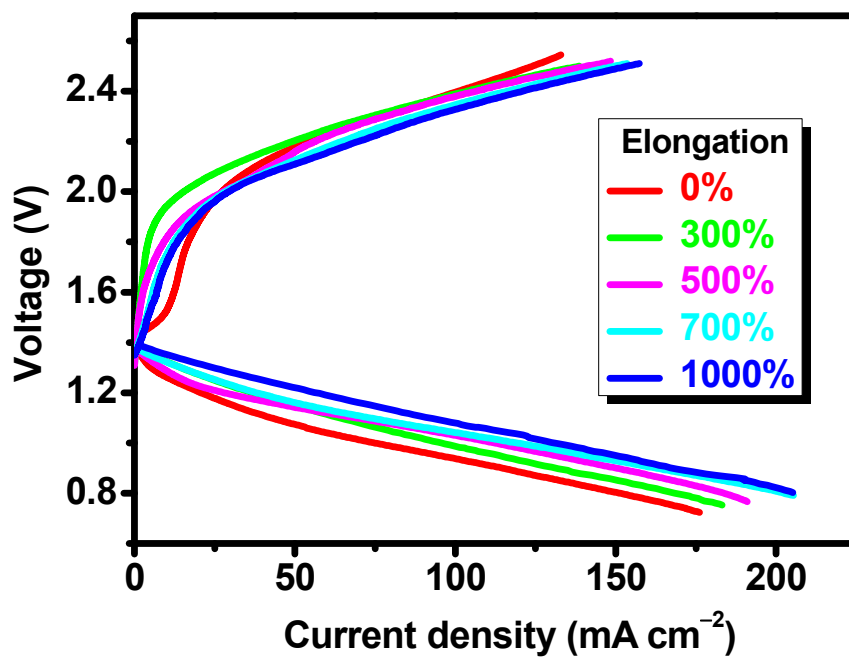
Fig. S35 Mechanical and electrochemical robustness of the stretchable ZAB. Polarization curves of the stretchable ZAB under various elongations.
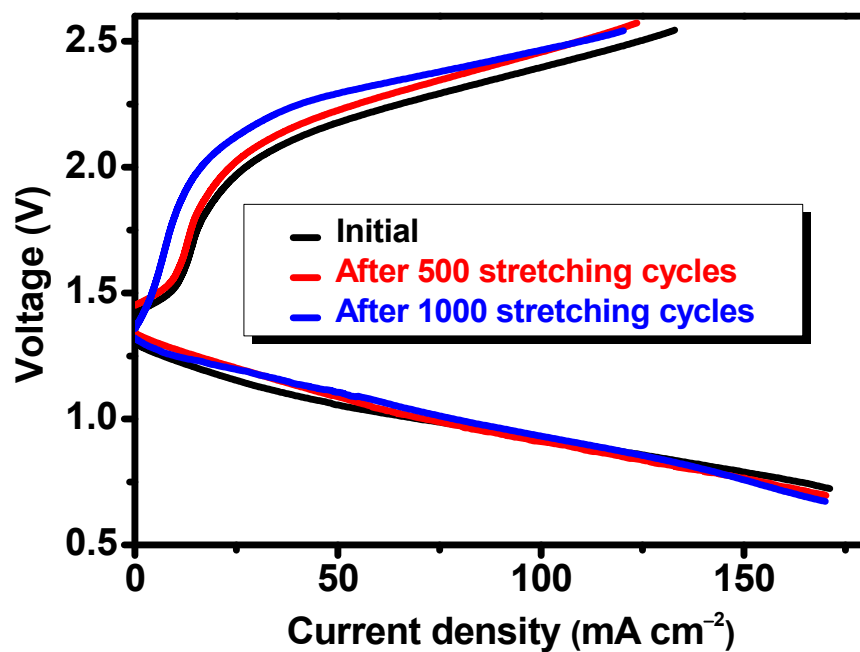
Fig. S36 Mechanical durability of the stretchable ZAB. a) Polarization curves and b) the stretchable ZAB before and after 500 and 1000 stretching cycles under 500% strain, respectively, demonstrating superior mechanical durability of the stretchable ZAB to withstand multiple stretching.
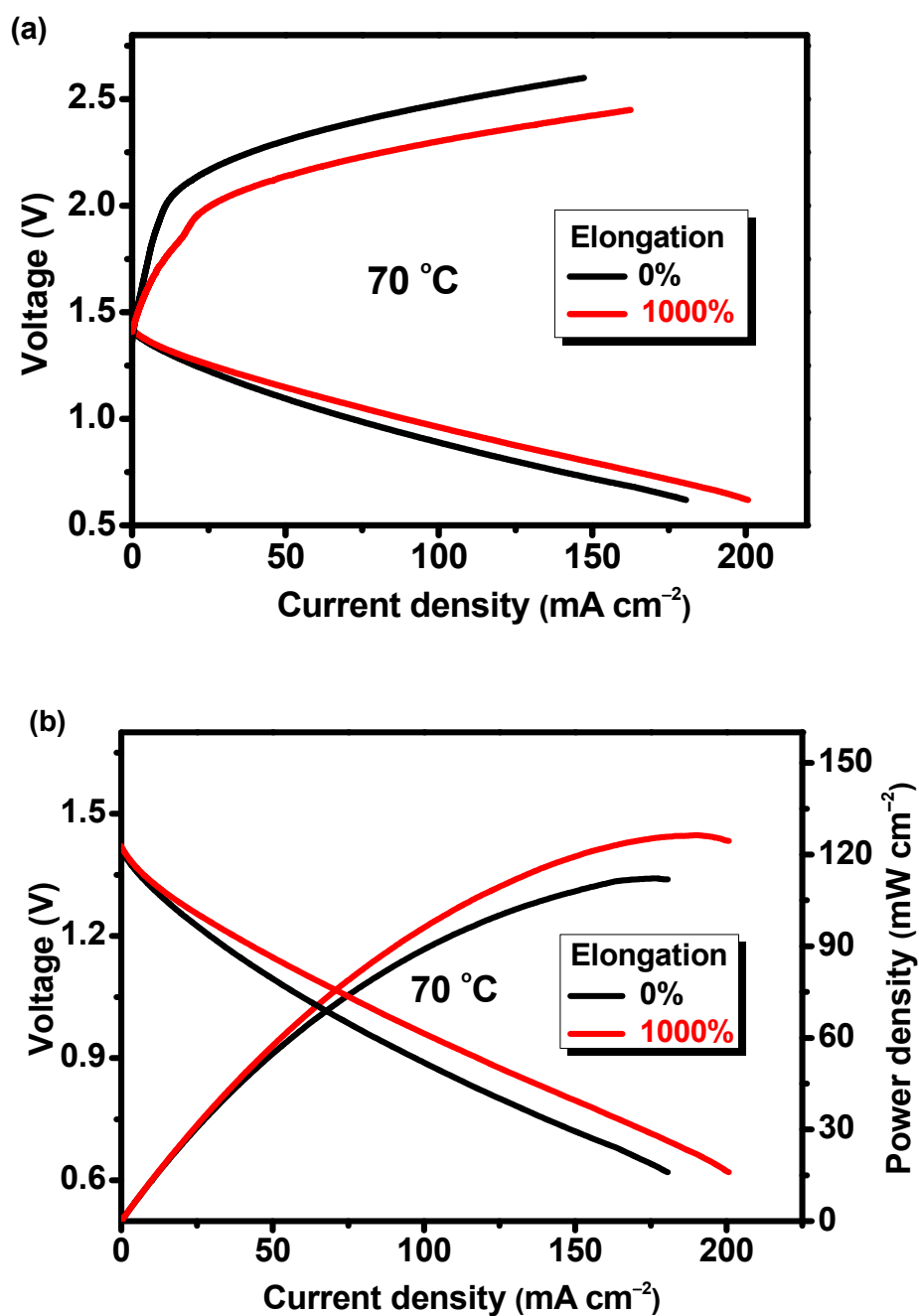
Fig. S37 High-temperature tolerance of the stretchable ZAB at 70 °C. a) Polarization curves and b) discharge profiles and the corresponding power density curves of the stretchable ZAB under the intial and 1000% stretching state, showing reliable electrochemical performance even being stretched up to 1000% strain at 70 °C.

(a)

(b)
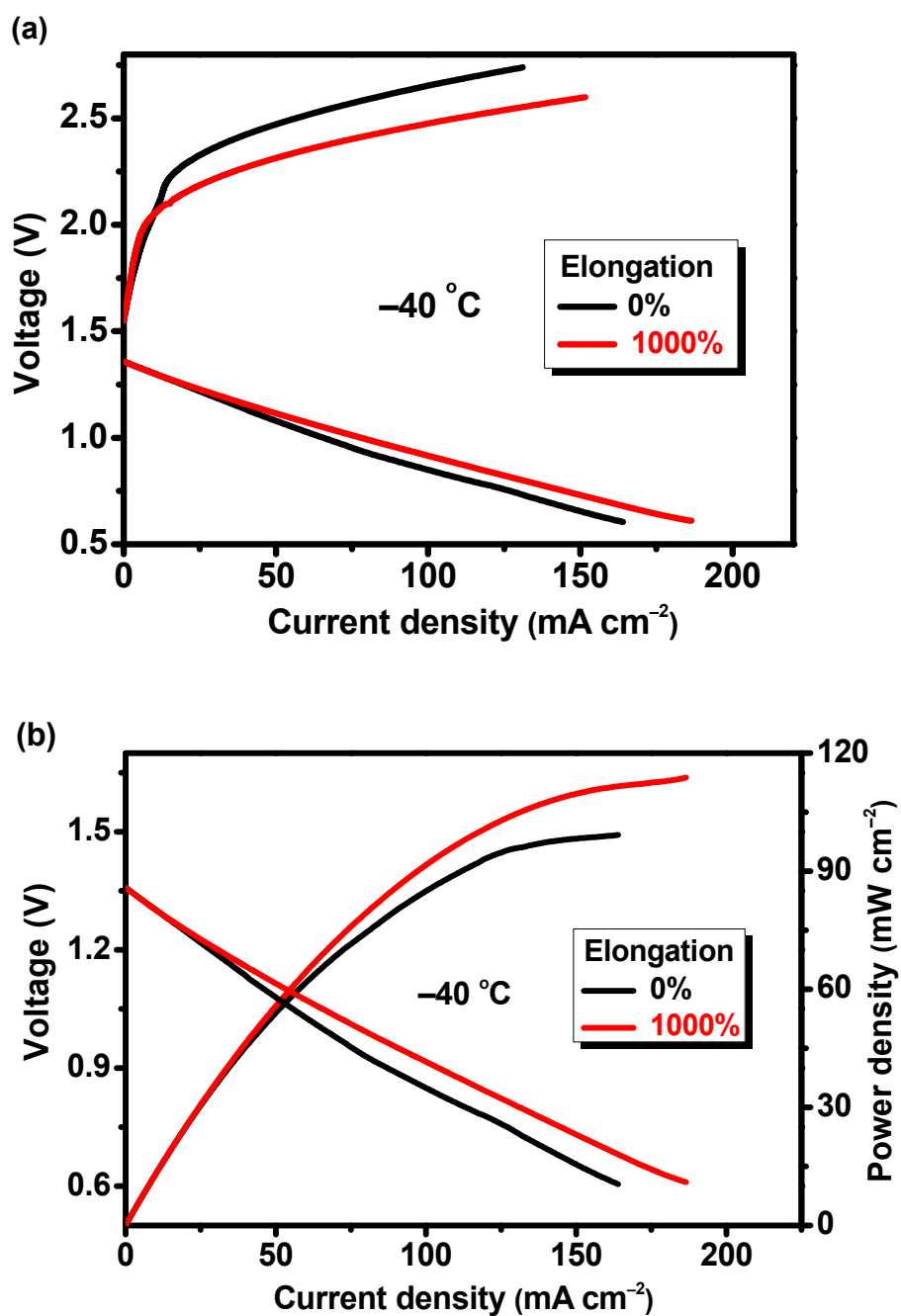
Fig. S38 Ultra-low temperature tolerance of the stretchable ZAB at –40 °C. (a) Polarization curves and (b) discharge profiles and corresponding power density curves of the stretchable ZAB under the intial and 1000% stretching state, showing reliable electrochemical performance even being stretched up to 1000% strain at –40 °C.

Table S11. Comparison of the electrochemical performance of the Zn–air battery in this work with those reported in the literature.

Gel electrolyte	OCV (V)	Power density (mW cm^{-2})	Cycling stability (h)	Stretchability	Operating temperature	*Refs.*
600% KOH (6 M)-filled G-CyBA/PAAm SP-DN hydrogel	**1.41**	**127.8**	**7**	**–**	**100 °C**	**This work**
	1.44	**136.9**	**32**	**> 1000%**	**70 °C**	
	1.47	**165.3**	**100**	**> 1000%**	**25 °C**	
	1.39	**107.6**	**48**	**> 1000%**	**–40 °C**	
	1.37	**96.9**	**40**	**–**	**–50 °C**	
KI-PVAA-GO hydrogel	ca. 1.4	78.6	200	–	RT	19
PANa-cellulose-6 M KOH hydrogel	1.47	>160	55	500%	RT	20
alkalified-PAA hydrogel	1.49	160.0	105		25 °C	22
	1.44	122.9	–	–	0 °C	
	1.40	80.5	–		–20 °C	
PAMPS-K25-MC2.0-5M KOH hydrogel	1.35	73.9	24		25 °C	23
	1.38	52.4	24	–	–20 °C	
(PAA)-KOH hydrogel	–	19.7	18	100%	RT	29
PVA gel-6 M KOH-0.2 M ZnCl$_2$ hydrogel	1.258	91.4	26	–	RT	30

(Continued)

Gel electrolyte	OCV (V)	Power density (mW cm^{-2})	Cycling stability (h)	Stretchability	Operating temperature	*Refs.*
PVA-KOH hydrogel	1.35	_	13.3	125%	RT	31
PAM/PAA-6 M KOH hydrogel	1.20 1.42 – 1.44	12.8 11.8 9.6 8.2	3 10 – –	–	70 °C 25 °C 0 °C –20 °C	32
PVA-KOH hydrogel	1.31	–	25	–	RT	33
PGEs-6 M KOH hydrogel	–	39	50	–	RT	34

Section S7   References

[1]   C. Gu, J. Li, J.-P. Liu, H. Wang, Y. Peng and C.-S. Liu, *Appl. Catal. B Environ.*, 2021, **286**, 119888.

[2]   A. Troć, J. Gajewy, W. Danikiewicz and M. Kwit, *Chem. Eur. J.*, 2016, **22**, 13258–13264.

[3]   J. J. P. Stewart, *J. Mol. Model.*, 2013, **19**, 1–32.

[4]   S. Grimme, S. Ehrlich and L. Goerigk, *J. Comput. Chem.*, 2011, **32**, 1456–1465.

[5]   M. J. Frisch, et al. Gaussian Incorporation, Wallingford, CT, USA 2016.

[6]   Q. Chen, D. Wei, H. Chen, L. Zhu, C. Jiao, G. Liu, L. Huang, J. Yang, L. Wang and J. Zheng, *Macromolecules*, 2015, **48**, 8003–8010.

[7]   J. Hu, K. Hiwatashi, T. Kurokawa, S. M. Liang, Z. L. Wu and J. P. Gong, *Macromolecules*, 2011, **44**, 7775–7781.

[8]   J. Deng, H. Yuk, J. Wu, C. E. Varela, X. Chen, E. T. Roche, C. F. Guo and X. Zhao, *Nat. Mater.*, 2021, **20**, 229–236.

[9]   J. Yang, R. Bai, B. Chen and Z. Suo, *Adv. Funct. Mater.*, 2020, **30**, 1901693.

[10]   L. Fang, Z. Cai, Z. Ding, T. Chen, J. Zhang, F. Chen, J. Shen, F. Chen, R. Li, X. Zhou and Z. Xie, *ACS Appl. Mater. Interfaces*, 2019, **11**, 21895–21903.

[11]   H. Zhang, W. Niu and S. Zhang, *Chem. Eng. J.*, 2020, **387**, 124105.

[12]   J. Zhang, L. Zeng, Z. Qiao, J. Wang, X. Jiang, Y. S. Zhang and H. Yang, *ACS Appl. Mater. Interfaces*, 2020, **12**, 30247–30258.

[13]   F. Chen, Z. Tang, S. Lu, L. Zhu, Q. Wang, Q. Gang, J. Yang and Q. Chen, *Polymer*, 2019, **168**, 159−167.

[14]   Y. Wang, F. Chen, Z. Liu, Z. Tang, Q. Yang, Y. Zhao, S. Du, Q. Chen and C. Zhi, *Angew. Chem. Int. Ed.*, 2019, **58**, 15707–15711.

[15]   Y. Yang, X. Wang, F. Yang, L. Wang and D. Wu, *Adv. Mater.*, 2018, **30**, 1707071.

[16]   J.-Y. Sun, X. Zhao, W. R. K. Illeperuma, O. Chaudhuri, K. H. Oh, D. J. Mooney, J. J. Vlassak and Z. Suo, *Nature*, 2012, **489**, 133–136.

[17]   H. Chen, Y. Liu, B. Ren, Y. Zhang, J. Ma, L. Xu, Q. Chen and J. Zheng, *Adv. Funct. Mater.*, 2017, **27**, 1703086.

[18]   T. L. Sun, T. Kurokawa, S. Kuroda, A. Bin Ihsan, T. Akasaki, K. Sato, M. A. Haque, T. Nakajima, J. P. Gong and *Nat. Mater.*, 2013, **12**, 932–937.

[19]   Z. Song, J. Ding, B. Liu, X. Liu, X. Han, Y. Deng, W. Hu and C. Zhong, *Adv. Mater.*, 2020, **32**, 1908127.

[20]   L. Ma, S. Chen, D. Wang, Q. Yang, F. Mo, G. Liang, N. Li, H. Zhang, J. A. Zapien and C. Zhi, *Adv. Energy Mater.*, 2019, **9**, 1803046.

[21]   Y. Bai, B. Chen, F. Xiang, J. Zhou, H. Wang and Z. Suo, *Appl. Phys. Lett.*, 2014, **105**, 151903.

[22]   Z. Pei, Z. Yuan, C. Wang, S. Zhao, J. Fei, L. Wei, J. Chen, C. Wang, R. Qi, Z. Liu and Y. Chen, *Angew. Chem. Int. Ed.*, 2020, **59**, 4793–4799

[23]   N. Sun, F. Lu, Y. Yu, L. Su, X. Gao and L. Zheng, *ACS Appl. Mater. Interfaces*, 2020, **12**, 11778–11788.

[24]   Y. Liang, L. Ye, X. Sun, Q. Lv and H. Liang, *ACS Appl. Mater. Interfaces*, 2020, **12**, 1577–1587.

[25]   H. Wang, J. Liu, J. Wang, M. Hu, Y. Feng, P. Wang, Y. Wang, N. Nie, J. Zhang, H. Chen, Q. Yuan, J. Wu and Y. Huang, *ACS Appl. Mater. Interfaces*, 2019, **11**, 49–55.

[26]   S. Li, H. Pan, Y. Wang and J. Sun, *J. Mater. Chem. A* 2020, **8**, 3667–3675.

[27]   X. P. Morelle, W. R. Illeperuma, K. Tian, R. Bai, Z. Suo and J. J. Vlassak, *Adv. Mater.*, 2018, **30**, 1801541.

[28]   X. Zhang, X. Ma, T. Hou, K. Guo, J. Yin, Z. Wang, L. Shu, M. He and J. Yao, *Angew. Chem. Int. Ed.*, 2019, **58**, 7366–7370.

[29]   S. Qu, B. Liu, J. Wu, Z. Zhao, J. Liu, J. Ding, X. Han, Y. Deng, C. Zhong and W. Hu, *ACS Appl. Mater. Interfaces*, 2020, **12**, 54833–54841.

[30]   H.-F. Wang, C. Tang, B. Wang, B.-Q. Li, X. Cui and Q. Zhang, *Energy Storage Mater.*, 2018, **15**, 124–130.

[31]   S. Qu, Z. Song, J. Liu, Y. Li, Y. Kou, C. Ma, X. Han, Y. Deng, N. Zhao, W. Hu and C. Zhong, *Nano Energy*, 2017, **39**, 101–110.

[32]   R. Chen, X. Xu, S. Peng, J. Chen, D. Yu, C. Xiao, Y. Li, Y. Chen, X. Hu, M. Liu, H. Yang, I. Wyman and X. Wu, *ACS Sustain. Chem. Eng.*, 2020, **8**, 11501–11511.

[33]   Y. Li, C. Zhong, J. Liu, X. Zeng, S. Qu, X. Han, Y. Deng, W. Hu and J. Lu, *Adv. Mater.*, 2018, **30**, 1703657.

[34]   M. J. Tan, B. Li, P. Chee, X. Ge, Z. Liu, Y. Zong and X. J. Loh, *J. Power Sources*, 2018, **400**, 566–571.